

Variability of quasilinear diffusion coefficients for plasmaspheric hiss

Article

Accepted Version

Watt, C., Allison, H., Meredith, N., Thompson, R., Bentley, S., Rae, I. J., Glauert, S. and Horne, R. (2019) Variability of quasilinear diffusion coefficients for plasmaspheric hiss. *Journal of Geophysical Research: Space Physics*, 124 (11). pp. 8488-8506. ISSN 2169-9402 doi: <https://doi.org/10.1029/2018JA026401> Available at <http://centaur.reading.ac.uk/86592/>

It is advisable to refer to the publisher's version if you intend to cite from the work. See [Guidance on citing](#).

To link to this article DOI: <http://dx.doi.org/10.1029/2018JA026401>

Publisher: American Geophysical Union

All outputs in CentAUR are protected by Intellectual Property Rights law, including copyright law. Copyright and IPR is retained by the creators or other copyright holders. Terms and conditions for use of this material are defined in the [End User Agreement](#).

www.reading.ac.uk/centaur

CentAUR

Central Archive at the University of Reading

Reading's research outputs online

Variability of Quasilinear Diffusion Coefficients for Plasmaspheric Hiss

C. E. J. Watt¹, H. J. Allison^{2,3,4}, N. P. Meredith², R. L. Thompson⁵, S. N.
Bentley¹, I. J. Rae⁶, S. A. Glauert², R. B. Horne²

¹Department of Meteorology, University of Reading, Reading, UK

²British Antarctic Survey, Cambridge, UK

³Department of Applied Mathematics and Theoretical Physics, University of Cambridge, UK

⁴now at GFZ German Research Centre for Geosciences, Potsdam, Germany

⁵Department of Mathematics and Statistics, University of Reading, Reading, UK

⁶Mullard Space Science Laboratory, University College London, UK

Key Points:

- We construct distributions of quasilinear diffusion coefficients for hiss using multiple simultaneous observations of input parameters
- Using realistic, observed variation of input parameters, diffusion coefficients at a specified energy exhibit large variance
- Distributions of diffusion coefficients are non-Gaussian, including when parameterized by specified ranges of AE-index

Corresponding author: Clare Watt, c.e.watt@reading.ac.uk

Abstract

In the Outer Radiation Belt, the acceleration and loss of high-energy electrons is largely controlled by wave-particle interactions. Quasilinear diffusion coefficients are an efficient way to capture the small-scale physics of wave-particle interactions due to magnetospheric wave modes such as plasmaspheric hiss. The strength of quasilinear diffusion coefficients as a function of energy and pitch-angle depends on both wave parameters and plasma parameters such as ambient magnetic field strength, plasma number density and composition. For plasmaspheric hiss in the magnetosphere, observations indicate large variations in the wave intensity and wavenormal angle, but less is known about the simultaneous variability of the magnetic field and number density. We use in-situ measurements from the Van Allen Probe mission to demonstrate the variability of selected factors that control the size and shape of pitch-angle diffusion coefficients: wave intensity, magnetic field strength and electron number density. We then compare with the variability of diffusion coefficients calculated individually from co-located and simultaneous groups of measurements. We show that the distribution of the plasmaspheric hiss diffusion coefficients is highly non-Gaussian with large variance, and that the distributions themselves vary strongly across the three phase-space bins studied. In most bins studied, the plasmaspheric hiss diffusion coefficients tend to increase with geomagnetic activity, but our results indicate that new approaches that include natural variability may yield improved parameterizations. We suggest methods like stochastic parameterization of wave-particle interactions could use variability information to improve modelling of the Outer Radiation Belt.

Plain Language Summary

The electrons in Earth's Radiation Belts exist in a highly rarefied part of space where collisions between particles is very rare. The only way in which the energy or direction of the trapped high-energy electrons can be changed is through interactions with electromagnetic waves. The efficacy of the interaction is a function of the energy and direction of travel of the electrons. In physics-based models of the Radiation belts, the efficacy of the wave-particle interactions is captured in diffusion coefficients. These functions are constructed from information about the amplitude and frequency properties of the waves in the interaction, and the magnetic field strength, ion composition and density of the local plasma. We build up collections of observations of these properties from multiple passes of one of the NASA Van Allen probes through the same three small regions of space. The observations display significant temporal variability. We report on the statistical distributions of wave intensity, magnetic field strength and plasma number density, and investigate the statistical distribution of the resulting diffusion coefficient. We find that the diffusion coefficients are highly variable and suggest that, by borrowing methods from other branches of geophysics such as numerical weather prediction, we may be able to include this variability in our models and improve the performance of Radiation Belt simulations.

1 Introduction

The radiation belts in the terrestrial magnetosphere are regions of high-energy trapped particles in near-Earth space. The inner belt is relatively stable and dominated by high-energy protons. The outer radiation belt exhibits strong variations in both the flux of high-energy electrons and in the extent of the region they inhabit (e.g. Miyoshi, Jordanova, Morioka, and Evans (2005)). A large contributor to the existence of the slot region between the belts (e.g. Meredith, Horne, Glauert, and Anderson (2007); Kim, Shprits, Subbotin, and Ni (2011)), and the rapid variations in the outer belt is wave-particle interactions across a wide range of frequencies (e.g. Thorne (2010); Horne, Meredith, Glauert, and Kersten (2016)). The challenge for modelling wave-particle interactions is that we

would like to construct a model of electron behaviour over hours, days and months when the underlying wave-particle interactions occur on timescales of microseconds to minutes. A powerful method of describing wave particle interactions over long timescales is the use of quasilinear theory to construct diffusion coefficients to encapsulate the micro-scale physics (e.g. Horne et al. (2005a)), before using these diffusion coefficients in macro-scale models (e.g. Horne et al. (2005b); Varotsou et al. (2008); Subbotin and Shprits (2009); Reeves et al. (2012); Glauert, Horne, and Meredith (2014a); Ma et al. (2015); Albert, Starks, Horne, Meredith, and Glauert (2016)). In these types of models, the diffusion coefficients can be considered to be descriptions of “sub-grid scale physics” and contain information regarding the strength of the wave-particle interaction as a function of energy E and pitch-angle α .

Diffusion coefficients D_{ij} can be constructed for interactions between electrons and waves across a wide range of frequencies important in the magnetosphere, from large-scale ultra-low frequency (ULF) waves (e.g. Fei, Chan, Elkington, and Wiltberger (2006); Lejosne, Boscher, Maget, and Rolland (2012); Ozeke, Mann, Murphy, Rae, and Milling (2014)) to higher frequency waves such as electromagnetic ion cyclotron waves (e.g. Kersten et al. (2014); Drozdov et al. (2017)) and whistler-mode waves (e.g. Ni, Thorne, Shprits, and Bortnik (2008); Albert, Meredith, and Horne (2009); Horne et al. (2013); Glauert, Horne, and Meredith (2013); Ripoll et al. (2016)). The diffusion coefficients depend strongly upon wave intensity, but also on parameters that can affect the efficiency and location in (E, α) space of the wave-particle interaction, such as frequency, wavenormal angle, local number density, composition, and ambient magnetic field strength.

Wave characteristics in the magnetosphere are highly variable across a wide range of different wave modes important for the radiation belts. The amplitude of whistler mode waves (Agapitov et al., 2013; Spasojevic et al., 2015; Malaspina et al., 2017; Watt et al., 2017) and the amplitude of ultra-low frequency (ULF) waves (Bentley et al., 2018a) demonstrate significant variability, even when binned by geomagnetic activity or other driving parameter. The wavenormal angle (Agapitov et al., 2013; Hartley et al., 2018) of whistler-mode waves, and the azimuthal wavenumber of ULF waves (Murphy et al., 2018) is also highly variable. Finally, the wave frequency range of whistler-mode waves has demonstrated variability (Meredith et al., 2007; Horne et al., 2013; Li et al., 2015). Additionally, it is important to remember that it is not only the wave characteristics that determine the strength of the wave-particle interaction (Horne et al., 2003b). For example, there is observational evidence that the efficiency of the electromagnetic ion-cyclotron wave-particle interaction can vary with time due to the variation in cold plasma number density, in addition to the variation in the wave properties (Blum et al., 2015).

Typically, diffusion coefficient models use average values of the wave characteristics, and augment these with models of the ambient magnetic field, plasma composition and number density (e.g. Subbotin and Shprits (2009); Fok et al. (2011); Glauert et al. (2013); Horne et al. (2013); Tu et al. (2013)). Models are constructed in phase-space, where a convenient co-ordinate system is based upon the adiabatic invariants μ , J and L^* . Diffusion coefficients are constructed by obtaining bounce- and drift-averaged models of the wave-particle interaction that are constrained by observations. While parameterized diffusion coefficients are generally adequate for understanding the overall dynamics of the radiation belts (e.g. Glauert, Horne, and Meredith (2018)), recent work has shown that event-specific diffusion coefficients can be used to examine specific intervals with greater success (Tu et al., 2014; Ripoll et al., 2016; Mann et al., 2016; Ripoll et al., 2017; Ma et al., 2018). It is important to note that the success of event-specific diffusion coefficient models highlights the large variability of wave-particle interactions possible in the radiation belts, and motivates our attempt to capture, describe and use this variability in future diffusion-based models.

The creation of event-specific diffusion models can capture extreme values and rapid variations that are not reproduced by the averaged parameterized models, however there

121 are some caveats to their use. Diffusion of drifting electrons in the radiation belts is a
 122 global phenomenon, and information regarding wave-particle interactions is required at
 123 all magnetic local times (MLT) in order to estimate the drift-averaged diffusion coeffi-
 124 cient. If one uses a small number of spacecraft to construct an event-specific diffusion
 125 model, then that model will not capture all of the variability in MLT and may result in
 126 under- or over-estimating the diffusion that results. More pressing is the knowledge that
 127 the NASA Van Allen Probes and JAXA Arase spacecraft are missions with finite life-
 128 times, and so event-specific information will not always be available in future, or for study-
 129 ing historical events prior to their launch. A parameterized model of diffusion coefficients
 130 therefore remains a valid goal.

131 We suggest that given the inherent variability of wave-particle interactions in the
 132 radiation belts, a modelling strategy such as stochastic parameterization (e.g. Berner
 133 et al. (2017)) is worth consideration. In these types of models, the parameterization of
 134 the diffusion coefficients is not deterministic, but probabilistic, and the variability of the
 135 wave-particle interactions is rigorously included. To apply a stochastic parameterization
 136 to wave-particle interactions in the radiation belts, we first need to characterize all as-
 137 pects of variability of the diffusion coefficients for each wave mode: the underlying dis-
 138 tribution of the variability, the size of the variance, the characteristic scales of tempo-
 139 ral and spatial variability and the existence of any caps or upper limits to diffusion. In
 140 this paper, we use observations from Van Allen probes to investigate the variability of
 141 diffusion due to plasmaspheric hiss. We will demonstrate the variability of the input pa-
 142 rameters for the calculation of the diffusion coefficient, and discuss the variability of a
 143 set of diffusion coefficients calculated from co-located and simultaneous measurements
 144 in small phase-space bins in the inner magnetosphere. We attempt to broadly identify
 145 the underlying distribution of each of the quantities we study, as well as estimate the size
 146 of the variability. Note that probabilistic models can be created quite efficiently if the
 147 underlying distribution is well-defined (e.g. normal or log-normal), since a small num-
 148 ber of parameters (e.g. mean and standard deviation or their equivalent) can be used to
 149 characterize the entire distribution.

150 We focus on plasmaspheric hiss as it is a wave mode ubiquitous to the high den-
 151 sity regions of the plasmasphere. It is straightforwardly identified in spacecraft obser-
 152 vations of electromagnetic wave spectra, with frequencies from tens of Hz to a few kHz
 153 (Li et al., 2015) that does not tend to feature rapid temporal structures in frequency spec-
 154 tra (e.g. Li, Thorne, Bortnik, Tao, and Angelopoulos (2012)). Plasmaspheric hiss is im-
 155 portant for losses of high-energy electrons in the inner magnetosphere through pitch-angle
 156 scattering (Meredith et al., 2006; Lam et al., 2007), and particularly for loss in the slot
 157 region (Meredith et al., 2007, 2009). Velocity-space diffusion due to plasmaspheric hiss
 158 is dominated by pitch-angle diffusion (Lyons et al., 1972) and so we study the variabil-
 159 ity of the pitch-angle diffusion coefficient $D_{\alpha\alpha}$ in this paper.

160 In this work, we use data from multiple instruments on board the NASA Van Allen
 161 Probes mission to quantify the range of pitch-angle diffusion coefficients active in the in-
 162 ner magnetosphere due to plasmaspheric hiss and relate them to diffusion coefficient val-
 163 ues calculated from the means or medians of the input parameters, such as plasma to
 164 gyro-frequency ratio, and wave intensity. We examine the underlying distributions of each
 165 input parameter, as well as the distribution of the resulting pitch-angle diffusion coef-
 166 ficients, and determine how varying each input parameter varies the diffusion coefficient.
 167 We will also determine how the probability distribution of hiss-mediated pitch-angle dif-
 168 fusion coefficients varies with increasing geomagnetic activity, since activity is often used
 169 to parameterize wave-particle interactions in the radiation belts (e.g. Horne et al. (2013)).
 170 In Section 2 we discuss the data sources and methods we will use to characterize the vari-
 171 ability of inputs to and outputs of the diffusion coefficient calculation using the British
 172 Antarctic Survey PADIE code (Glauert & Horne, 2005). Section 3 demonstrates the vari-
 173 ability of the inputs independently, before we show the variability of the resulting dif-

174 fusion coefficients in Section 4. We discuss the implications of results for modeling wave-
 175 particle interactions in the radiation belts in Section 5, and conclude in Section 6.

176 2 Data and Methods

177 2.1 Input parameters

178 We use simultaneous and co-located data from different instruments on the NASA
 179 Van Allen Probes mission to study the distribution of quasilinear diffusion coefficients.
 180 Our intention here is to illustrate, using a few examples, the variability that may be present
 181 in diffusion coefficients due to plasmaspheric hiss, and to evaluate whether our analy-
 182 sis should be extended in future work. It is important to note that the calculation of dif-
 183 fusion coefficients is computationally expensive, and so we choose a small number of ex-
 184 ample bins in this illustrative study. We select three small bins in the inner magneto-
 185 sphere that are predominantly inside the plasmasphere and in the morning sector, where
 186 hiss has been shown to be present (Meredith et al., 2004, 2018). It's equally important
 187 to note that the extent of the phase-space bin used to collate observations when construct-
 188 ing a diffusion model is a source of potential variability; too large a bin, and we run the
 189 risk of conflating wave activity and plasma properties from different regions of the mag-
 190 netosphere, whereas too small a bin can lead to small numbers of observations and a sta-
 191 tistically poor sample. Thanks to the excellent coverage of the Van Allen probes over
 192 the > 3 year period used, we have > 1500 data points in each of the relatively small
 193 bins used (see description below). We hope to minimise any potential variations due to
 194 radial and azimuthal location, and note that future, more comprehensive, models can
 195 help determine the most appropriate resolution, or indeed coordinate system, to use when
 196 building an observationally-constrained diffusion coefficient model.

197 We choose a phase-space coordinate system that is tied to electron adiabatic be-
 198 haviour in the magnetosphere, i.e. we bin our observations in L^* where it has been cal-
 199 culated using the Olson-Pfizer quiet time model (Olson & Pfizer, 1977) with the Inter-
 200 national Geomagnetic Reference Field (IGRF) for the middle of the appropriate year.
 201 Since L^* is defined for particles, but we here use it for waves, we assume a local pitch
 202 angle of $\alpha = 90^\circ$ for this calculation. We also restrict our observations to those that
 203 are in a small section of magnetic local time (MLT) and magnetic latitude λ_m (where
 204 $\lambda_m = 0$ at the magnetic equator). We focus on plasmaspheric hiss and so choose three
 205 L^* ranges that are predominantly inside the plasmasphere: $2.45 < L^* < 2.55$, $2.95 <$
 206 $L^* < 3.05$ and $3.45 < L^* < 3.55$ (these bins will be referred to as the $L^* = 2.5$ bin,
 207 the $L^* = 3.0$ bin and the $L^* = 3.5$ bin, respectively). Narrow bin sizes are chosen in
 208 an attempt to minimize any variation of diffusion coefficient with L^* . Similarly, we choose
 209 a narrow range of 0900-1000 MLT for all three regions, and a narrow range of magnetic
 210 latitude $0 < \lambda_m < 6^\circ$, as wave and plasma parameters are known to be MLT and lat-
 211 itude dependent (Meredith et al., 2004, 2018).

212 Our aim is to use co-located and simultaneous measurements of key inputs for the
 213 diffusion coefficient calculation in order to determine the variability of diffusion in each
 214 chosen plasmaspheric bin. Ripoll et al. (2017) have recently demonstrated the impor-
 215 tance of using such simultaneous observations of multiple input parameters in order to
 216 more accurately determine the quasilinear diffusion coefficients during specific events.
 217 Coefficients for the interaction between plasmaspheric hiss and electrons (e.g. equations
 218 (11-13) in Glauert and Horne (2005)) depend upon the local magnetic field strength $|B|$
 219 (through the electron gyrofrequency $\Omega_e = |q_e||B|/m_e$) and the local electron number
 220 density n_e (through the electron plasma frequency $\omega_{pe} = (n_e q_e^2 / \epsilon_0 m_e)^{1/2}$). Here, q_e and
 221 m_e are the electron charge and mass, respectively, and ϵ_0 is the electric permittivity of
 222 free space. They also depend upon the intensity of the waves δB^2 , and the dependence
 223 of the intensity on frequency ω and wavenormal angle ψ . In order to simplify our anal-
 224 ysis for our initial study of the variability of quasilinear diffusion coefficients, we will fo-

cus on the impact of variability in two important input parameters: wave intensity δB^2 and the ratio of plasma to gyrofrequency $\omega_{pe}/\Omega_e = f_{pe}/f_{ce}$, where $f_{pe} = \omega_{pe}/(2\pi)$ and $f_{ce} = \Omega_e/(2\pi)$. We therefore fix the shape of the input wave spectra, and vary only the wave intensity at $f = 252$ Hz. This frequency is chosen as it is close to the peak of the statistical average wave spectra as determined by Li et al. (2015). We stress that it is very important to use co-located and simultaneous measurements of input parameters in order to capture the true variability of diffusion coefficients (c.f. Ripoll et al. (2017)). Future work will consider the effects of variability in the observed dependence of δB^2 on ω and ψ , the local ion composition, and the dependence of input wave parameters on magnetic latitude.

For this study we used data from the Van Allen probe A. The Van Allen probes were launched on 30 August 2012 into highly elliptical orbits with a perigee of 618 km, an apogee of 30,414 km and an inclination of 10.2° . The orbital period is 537.1 minutes. The satellites sweep through the plasmasphere approximately 5 times per day, making them excellent probes of this important region.

We use data from the Electric and Magnetic Field Instrument Suite and Integrated Science (EMFISIS)(Kletzing et al., 2013) on board Van Allen probe A. We use the Waveform Receiver (WFR) for measurements of the wave magnetic field. This instrument provides measurements of all three components of the wave electric and magnetic fields in 65 frequency channels in the frequency range from 10 Hz to ~ 12 kHz every 6 seconds. Specifically we use the WNA survey data product for the sum of the three components of the wave magnetic field and the ellipticity. Concomitant measurements of the electron gyrofrequency f_{ce} are determined from the 1s fluxgate magnetometer data. The co-located measurements of the electron plasma frequency are determined from the High Frequency Receiver (HFR). This instrument provides measurements of one component of the electric field in the plane perpendicular to the spin axis in 82 logarithmically-spaced frequency bins in the frequency range 10-400 kHz every 6s. The electron plasma frequency f_{pe} , which is provided as a L4 density product, is derived from the lower hybrid resonance frequency when visible, or the lower frequency limit of the continuum radiation (Kurth et al., 2015).

Many wave parameters are required as input for the diffusion coefficient (see e.g. Glauert and Horne (2005)). However, we model the variability of the waves using only one variable - the intensity of emission at $f = 252$ Hz which is used to constrain the peak of the frequency distribution in the diffusion coefficient calculation (see section 2.2). Li et al. (2015) demonstrate that the statistical hiss frequency spectrum peaks at this frequency for low L .

To compile the subset of data required in our study, we sequentially analyzed each day of Van Allen probe A data from 15 September 2012 until 12 February 2016. We stored co-located measurements of plasmaspheric hiss wave power spectral density at $f = 252$ Hz, f_{ce} , f_{pe} , UT date and time, magnetic latitude, magnetic local time and geomagnetic activity as monitored by the AE index as a function of half orbit, L^* , in steps of $0.1L^*$, and observation number in that bin. For our chosen location bins we then extracted and stored each co-located measurement of the wave power spectral density at $f = 252$ Hz, f_{pe} , f_{ce} and the corresponding AE index. These measurements are used to first construct probability density functions of the input parameters for the diffusion coefficient calculation f_{pe}/f_{ce} and wave intensity, and the probability distributions of the underlying physical parameters like magnetic field and number density that feed into the input f_{pe}/f_{ce} ratio (see section 3). Diffusion coefficients are then calculated using the method described in section 2.2 and their probability distributions displayed in section 4.

Note that plasmaspheric hiss can overlap in frequency with magnetosonic waves (Russell et al., 1970; Santolík et al., 2004) and whistler mode chorus (Koons & Roeder, 1990; Tsurutani & Smith, 1977). We excluded periods of magnetosonic waves, which typ-

277 ically have large wave normal angles and hence low ellipticity values, by excluding waves
 278 with ellipticity less than 0.7. Plasmaspheric hiss tends to be confined to high-density re-
 279 gions associated with the plasmasphere (e.g., Thorne, Smith, Burton, and Holzer (1973))
 280 and plasmaspheric plumes (e.g., Summers et al. (2008)), whereas whistler mode chorus
 281 waves are largely confined to the low-density region of the plasma trough (Tsurutani &
 282 Smith, 1977; Meredith et al., 2001). We further excluded probable observations of whistler
 283 mode chorus by restricting the co-located measurements to those observed inside the plasma-
 284 pause. We applied the number density threshold adopted by Sheeley, Moldwin, Rassoul,
 285 and Anderson (2001) to separate measurements likely made inside the plasmasphere, and
 286 those likely made outside. Figure 1 shows the distribution of observations in f_{pe} and f_{ce}
 287 for each of the three volume bins studied. The solid line indicates the number density
 288 threshold used by Sheeley et al. (2001). In Figure 1, observations that lie above each mod-
 289 eled line are deemed to be inside the plasmasphere, and are used in the subsequent anal-
 290 ysis. Over the ~ 3.5 years of Van Allen Probes coverage used in this study from 15 Septem-
 291 ber 2012 until 12 February 2016, this provides us with 1570 points in the $L^* = 2.5$ bin,
 292 2377 in the $L^* = 3.0$ bin, and 3272 in the $L^* = 3.5$ bin.

Figure 1: Occurrence of observations of plasma frequency and plasma gyrofrequency in different regions of the inner magnetosphere. Color indicates number of observations, horizontal dashed line indicates a condition on the number density for measurements inside (above) and outside (below) the plasmopause. (a) $L^* = 2.5$ bin, (b) $L^* = 3.0$ bin and (c) $L^* = 3.5$ bin

293 2.2 Diffusion coefficient calculation

294 We use the Pitch Angle and Energy Diffusion of Ions and Electrons (PADIE) code
 295 (Glauert & Horne, 2005) in order to calculate bounce-averaged pitch-angle scattering dif-
 296 fusion coefficients $D_{\alpha\alpha}$ for each of our pairs of co-located measurements. PADIE calcu-
 297 lates relativistic quasi-linear pitch-angle and energy diffusion coefficients for resonant wave-
 298 particle interactions in a magnetized plasma. The method requires multiple inputs that
 299 can be obtained from observations - the plasma number density and ion composition,
 300 magnetic field strength, an estimate of wave intensity dependence on frequency and wavenor-
 301 mal angle, upper and lower frequency cut-offs, upper and lower cut-offs of wavenormal
 302 angle, the latitudinal extent of the waves and finally the wave intensity. As mentioned
 303 above, we will restrict our analysis in this paper to the variability of $D_{\alpha\alpha}$ in response
 304 to natural variability in just two of those inputs - the plasma frequency to gyrofrequency
 305 ratio f_{pe}/f_{ce} , and the intensity of the waves. In this way we hope to show an illustra-
 306 tion of the variability of the estimated diffusion coefficients when two of the input pa-
 307 rameters are varied in a realistic way. The remaining inputs to the PADIE calculations
 308 are fixed as follows. We endeavour to use realistic values for the low-L region of the in-
 309 ner magnetosphere in this study, but note that simplifying choices have often been made
 310 to illustrate our point.

311 For the dependence of the hiss waves on frequency we fit a single Gaussian to the
 312 function given by (Li et al., 2015) for $L = 3$ to obtain an estimate of a reasonable plas-
 313 maspheric hiss spectra. The peak frequency of this spectrum is $f_{peak} = 252$ Hz, and
 314 the width $f_w = 194$ Hz. Note that this is a simplification of the function given by Li
 315 et al. (2015) for ease of use in the PADIE method, but is a reasonable estimate of the
 316 statistical hiss spectrum found therein. This information is then used to construct power
 317 spectral density

$$B^2(f) = \begin{cases} A^2 \exp\left(-\left(\frac{f-f_{peak}}{f_w}\right)^2\right), & \text{for } f_{lc} \leq f \leq f_{uc} \\ 0, & \text{otherwise} \end{cases} \quad (1)$$

where A^2 is the peak wave spectral intensity, and $f_{lc} = 100$ Hz, $f_{uc} = 2$ kHz are the lower and upper frequency cut-offs respectively. Cut-off values are chosen in reference to previous work on diffusion caused by plasmaspheric hiss (e.g. Ni, Bortnik, Thorne, Ma, and Chen (2013); Ni et al. (2014); Meredith et al. (2009)). We experimented with a lower value for $f_{lc} = 20$ Hz, since Li et al. (2015) indicate that wave spectral intensity can extend well below 100Hz, especially on the dayside. However, changing the lower cut-off frequency made little difference to the values obtained here for $D_{\alpha\alpha}$, similar to results shown by Li et al. (2015). Peak wave spectral intensity A^2 is supplied by each observation of the wave spectral intensity at $f = 252$ Hz.

The wavenormal angle dependence of the plasmaspheric hiss is also simplified for this analysis. Near the geomagnetic equator, plasmaspheric hiss has been reported to propagate predominately parallel to the geomagnetic field, while at higher latitudes more oblique propagation is observed (Ni et al., 2014; Chen et al., 2012). In addition, Hartley et al. (2018) demonstrate that the distribution of wavenormal angles for plasmaspheric hiss is sometimes bimodal. We choose to use a Gaussian function in $\tan \phi$, where ϕ is the wavenormal angle, similarly to Ni et al. (2014). As mentioned above, we restrict our analysis to a small range of magnetic latitude, and so we use the wave normal angle distribution provided by Ni et al. (2014) for waves observed from 0–5° magnetic latitude (i.e. $\phi_{lc} = 0^\circ$ and $\phi_{uc} = 20^\circ$). The wave normal angle distribution peak is set $\phi_{peak} = 0^\circ$, and the width $\phi_w = 15^\circ$. The wavevector magnitude $|k|$ is then calculated internally by PADIE using the magnetized cold plasma dispersion relation as discussed by Glauert and Horne (2005). An example of the refractive index $\mu = c|k|/\omega$ calculated during a single diffusion coefficient calculation, where c is the speed of light in a vacuum and $\omega = 2\pi f$, is shown in Figure S1 of the supplementary information.

The choices above motivate the latitudinal extent of waves used in the bounce-averaged calculations of PADIE, and so we restrict the latitudinal extent of the waves to $\lambda_{max} = 5^\circ$. Finally, the plasma composition is chosen and fixed to be an electron-proton plasma (i.e. in this analysis we ignore any heavier ion populations), and we restrict the number of resonances included in the calculations to the range $-10 < n < 10$. The relatively large number of resonances used in our calculation ensures that we capture the variability in $D_{\alpha\alpha}$ due to variability of input parameters, and not because we have inadvertently omitted small but important contributions from higher n resonances.

2.3 Measures of variability

The focus of this paper is to compare the variability in the input parameters for the diffusion coefficient calculation, and in the resulting diffusion coefficients themselves, so we choose the coefficient of variation c as our metric of variability. This standard statistical device is a normalized measure of the variability in different datasets. It is important to note that c takes different forms depending on the underlying distribution of the data. For normally-distributed data, the coefficient of variation is

$$c = \frac{\sigma}{\mu}, \quad (2)$$

where σ is the standard deviation of the data, and μ is the mean, and for log-normally distributed data

$$c = \sqrt{e^{\sigma_{ln}^2} - 1}, \quad (3)$$

Table 1: Number of observations used to estimate probability densities for each activity level.

L^*	$AE < 50$ nT	$50 < AE < 100$ nT	$100 < AE < 150$ nT	$AE > 150$ nT
2.5	800	381	239	150
3.0	1055	534	349	439
3.5	1387	695	801	389

where σ_{\ln} is the standard deviation of the natural logarithm of the data. Of course, magnetospheric data are rarely normally, or log-normally distributed, but a visual inspection of the data in each volume bin indicates that they resemble one or other of those forms sufficiently that the coefficient of variation is a reasonable measure of the variability and a good way to compare the variability of parameters with different units. Hence we will use the above definitions of c as required. Interpretation of the values of c is relatively straightforward; if $c < 1$, then the data exhibits low variance, but if $c > 1$, then the data are highly variable.

3 Variability of observed input parameters

In all the analysis that follows, we present the variability of all the input data used to calculate the quasilinear diffusion coefficients, and analyze the variability for increasing geomagnetic activity. The temporal variability of diffusion coefficients is often captured using some measure of geomagnetic activity (e.g. Spasojevic et al. (2015); Meredith et al. (2018)). We use AE so that results may be compared with previous work (e.g. Meredith et al. (2018)). The activity bins used are $AE < 50$ nT, $50 < AE < 100$ nT, $100 < AE < 150$ nT, and $AE > 150$ nT. Because the occurrence of high values of activity is low, the highest activity bin includes a much wider range of activity than the other three. However, the ranges chosen should be sufficient to show any trends if they exist in the data. Table 1 shows the number of data points in each activity bin in our analysis. We have chosen to ensure that we have sufficient data coverage in each activity bin, rather than isolate the small number of very high values of geomagnetic activity. This compromise is necessary due to the small volume bins that we have chosen to minimize any variations due to radial locations. Future analyses may utilize larger volume bins as appropriate in order to get better resolution in geomagnetic activity parameter space.

Figure 2: (a-c) Normalized histograms showing probability density of magnetic field strength measurements in each of the three volumes studied. (d-f) Estimate of the probability density using a kernel density estimate for different ranges of AE (see legend)

The variability in magnetic field strength for all of the data in our study is indicated in Figure 2. The top row of the figure indicates a histogram of all the magnetic field strength data used in the study. The variability of magnetic field strength as a function of geomagnetic activity can be seen in the second row of Figure 2. Here we have used a kernel density estimate to provide an estimate of the probability distribution function for different values of activity. The solid black line indicates the lowest activity bin $AE < 50$ nT, the dotted blue line indicates $50 < AE < 100$ nT, short dashed orange lines indicate $100 < AE < 150$ nT, and long dashed pink lines indicate $AE > 150$ nT. There

395 is not much variation in the distributions of magnetic field strength for increasing ge-
 396 omagnetic activity except at $L^* = 3.5$, where the highest range of AE corresponds to
 397 a slight shift in the probability density estimate towards lower values. As a "sanity check",
 398 we see that the average value of the magnetic field strength decreases with L^* .

399 For $L^* = 3.0$ and $L^* = 3.5$, the distribution appears fairly normal when inspected
 400 by eye. For $L^* = 2.5$, the distribution is more negatively skewed, yet the mean and stan-
 401 dard deviation are still reasonable statistical measures of the distribution. As a result,
 402 we will use equation (2) to calculate the coefficient of variation for the magnetic field strength.
 403 We discover that $c \sim 0.04$ at all locations and for all values of geomagnetic activity stud-
 404 ied here, which means that the standard deviation of the magnetic field strength mea-
 405 surements is less than 5% of the observed mean values.

Figure 3: (a-c) Normalized histograms showing probability density of number density estimates in each of the three volumes studied. (d-f) Estimate of the probability density using a kernel density estimate for different ranges of AE (see legend)

406 Figure 3 indicates the variability of number density, in the same format as Figure
 407 2. As described in Section 2.1, the number density is estimated from the value of the up-
 408 per hybrid frequency as detected by the Van Allen probe EMFISIS instrument. The data
 409 are unavoidably discretized due to the size of the finite frequency bins employed by EM-
 410 FISIS. Nonetheless, the histogram and kernel density estimates of probability density
 411 give us a good indication of the underlying distribution of the measurements. A brief
 412 "sanity check" indicates that the mean observed number density decreases with L^* . The
 413 distributions do not have a simple form, but they appear normal enough that the mean
 414 and standard deviation are useful statistical characterizations of these data. Hence we
 415 use equation (2) to calculate the coefficient of variation for number density, and discover
 416 that the variability is larger than for the magnetic field strength, with $c = 0.31$ at $L^* =$
 417 2.5 , $c = 0.35$ at $L^* = 3.0$ and $c = 0.39$ at $L^* = 3.5$. As geomagnetic activity in-
 418 creases, there are no systematic changes in number density observations. At $L^* = 2.5$,
 419 the shape of the distribution changes markedly (but not systematically) with increas-
 420 ing geomagnetic activity, and the variability of decreases markedly for $50 < AE < 100$ nT.
 421 It is interesting that the overall range of measurements is largely unchanged with increas-
 422 ing activity levels. At $L^* = 3.0$, the measured number density exhibits very little change
 423 with increasing magnetic activity until the highest levels are reached. At high levels of
 424 activity, the variability dramatically decreases, while the mean remains similar. Finally,
 425 there is little change in the distribution of number density values at $L^* = 3.5$ with in-
 426 creasing activity until the highest levels are reached; then the distribution of number den-
 427 sity observations is much more skewed towards lower values. In summary, for all L^* , there
 428 are no systematic changes in the distribution shape or range for number density at these
 429 selected locations.

Figure 4: (a-c) Normalized histograms showing probability density of f_{pe}/f_{ce} in each of the three volumes studied. (d-f) Estimate of the probability density using a kernel density estimate for different ranges of AE (see legend)

430 We combine co-located and simultaneous measurements of magnetic field strength
 431 and electron number density into the ratio f_{pe}/f_{ce} for use as an input to the PADIE cal-
 432 culations. The variability of this input parameter is shown in Figure 4 in the same for-

433 mat as for the magnetic field strength and number density analyses. The histograms indicate
 434 that the values of f_{pe}/f_{ce} at all locations studied are relatively normally distributed
 435 with well-defined means and standard deviations. The mean value of f_{pe}/f_{ce} increases
 436 with L^* . The variation of this parameter with increasing geomagnetic activity mirrors
 437 the patterns seen in Figure 3 for number density. Since f_{pe} varies with the square root
 438 of electron number density, the coefficient of variation for this PADIE input parameter
 439 is reduced from the variability seen for electron number density itself: $c = 0.16$ at $L^* =$
 440 2.5 , $c = 0.19$ at $L^* = 3.0$ and $c = 0.21$ at $L^* = 3.5$, all calculated using equation (2).

Figure 5: (a-c) Normalized histograms showing probability density of wave intensity at $f = 252$ Hz in each of the three volumes studied. (d-f) Estimate of the probability density using a kernel density estimate for different ranges of AE (see legend)

441 The second input for the PADIE calculations is the intensity of plasmaspheric hiss
 442 δB^2 at $f = 252$ Hz (see Section 2.2). Figure 5 shows the variability of this input pa-
 443 rameter in the same format as above. In this instance, wave intensities are presented on
 444 a logarithmic scale, and the probability density estimates are calculated for $\log_{10}(\delta B^2)$.
 445 The wave intensity data is presented in this form to highlight the logarithmic nature of
 446 the distribution, although it's important to note that the input parameter we use in the
 447 diffusion coefficient calculation in section 4 is δB^2 as required (Glauert & Horne, 2005).
 448 For all data (Figure 5a-c), the distribution of wave intensities does not have a simple form,
 449 but it is fair to say that they are highly non-Gaussian. At first glance, the distribution
 450 is closest to log-skew-normal with negative skew, and there is some evidence of multi-
 451 modal structure at $L^* = 2.5$ and $L^* = 3.0$. We should note here that there are some-
 452 where between 1500 and 2500 data points in each location bin. Given the size of the vari-
 453 ability in this parameter, and the non-Gaussian nature of the distribution, it may be un-
 454 wise to read too much into the details of the histograms.

455 Once we split the data by activity level, we observe that the strength of the waves
 456 tends to increase with geomagnetic activity. This is unsurprising, as the arithmetical av-
 457 erage of the wave intensity in similar location bins increases with increasing activity (e.g.
 458 Meredith et al. (2004, 2018)). Note however that there is significant overlap between the
 459 probability density estimates. At $L^* = 3.0$ and $L^* = 3.5$ there does appear to be a
 460 thresholding effect during increasing geomagnetic activity, rather than a gradual increase
 461 in wave intensity as the geomagnetic activity increases. At both locations, the proba-
 462 bility density estimates for $AE < 50$ nT and $50 < AE < 100$ nT are very similar, and
 463 the probability density estimates for $100 < AE < 150$ nT and $AE > 150$ nT are also
 464 very similar. Between the two lower activity levels and the two higher ones, there is a
 465 marked shift to the right in the distributions. Due to the logarithmic nature of the dis-
 466 tributions, we use equation (3) to calculate the coefficient of variation here, with $c =$
 467 5.8 at $L^* = 2.5$, $c = 9.7$ at $L^* = 3.0$, and $c = 5.8$ at $L^* = 3.5$. The amount of vari-
 468 ance is much larger for the wave intensities than it is for the plasma or ambient mag-
 469 netic field inputs.

Figure 6: One-dimensional probability functions of the wave intensity at $f = 252$ Hz as a function of f_{pe}/f_{ce} . The integral of each column in each panel is one. (a) $L^* = 2.5$ bin, (b) $L^* = 3.0$ bin and (c) $L^* = 3.5$ bin

470 It is important to discuss whether the two chosen inputs are independent. We con-
 471 struct a probability distribution function of the measured wave intensity at $f = 252$ Hz
 472 as a function of f_{pe}/f_{ce} . In Figure 6, every column in each of the three panels integrates
 473 to one (c.f. Figure 3 of Kellerman and Shprits (2012) and Figure 5 of Murphy et al. (2018)).
 474 There are no strong patterns in the dependence of wave intensity on frequency ratio at
 475 $L^* = 3.0$ or $L^* = 3.5$. There is a slight upwards trend for $L^* = 2.5$, although in all
 476 cases, the spread of measurements is large. The knowledge that the two inputs we pro-
 477 pose to study in the calculation of diffusion coefficients are effectively independent will
 478 aid our interpretation of the results.

479 Recent investigations of hiss amplitude across a range of radial locations in the mag-
 480 netosphere indicates that in some places, hiss amplitude varies more strongly with lo-
 481 cal number density than with radial location (Malaspina et al., 2018). For small L , these
 482 recent findings indicate that the variation of plasmaspheric hiss with number density is
 483 quite flat, and it is only at lower density (larger radial distance) that the variation be-
 484 comes large. This echoes what we see in Figure 6 where there seems little dependence
 485 of wave amplitudes on the plasma frequency to gyrofrequency ratio. However, the re-
 486 sults of Malaspina et al. (2018) indicate that input parameters for diffusion coefficient
 487 calculations may be interdependent in other parts of the inner magnetosphere.

488 4 Variability of $D_{\alpha\alpha}$

Figure 7: [top row] Normalized histograms showing probability density of $D_{\alpha\alpha}$ for
 $E = 0.5$ MeV and $\alpha = 30^\circ$ in each of the three volumes studied. [bottom row] Esti-
 mate of the probability density using a kernel density estimate for different ranges of AE
 (see legend)

489 First, we study the variability of the pitch-angle diffusion coefficient $D_{\alpha\alpha}$ at a sin-
 490 gle energy and pitch-angle, $E = 0.5$ MeV and $\alpha = 30^\circ$, chosen because $D_{\alpha\alpha}$ is shown
 491 to be strong at this energy and pitch-angle in previous analyses (e.g. Glauert et al. (2014a)).
 492 For each pair of co-located and contemporaneous observations of $\delta B^2(f = 252\text{Hz})$ and
 493 f_{pe}/f_{ce} , we calculate the value of $D_{\alpha\alpha}(E = 0.5\text{Mev}, \alpha = 30^\circ)$. Figure 7 shows the vari-
 494 ability of the resulting $D_{\alpha\alpha}$. The histograms of $D_{\alpha\alpha}$ are displayed on a logarithmic scale
 495 to demonstrate the nature of the variability. The median, upper and lower quartiles are
 496 also indicated with vertical lines. Like the distributions of δB , the distribution of $D_{\alpha\alpha}$
 497 appears closest to a log-skew-normal with negative skew. The median is always less than
 498 the mode, which often coincides with the upper quartile. However, the variability changes
 499 dramatically between the three chosen location bins. At $L^* = 2.5$, the variability is very
 500 large, with a long tail of very small values. The variability is less at higher L^* , although
 501 the distributions do exhibit the same underlying log-skew-normal pattern. The distri-
 502 butions of $D_{\alpha\alpha}$ at $L^* = 3.0$ and $L^* = 3.5$ are very similar in shape, although the me-
 503 dian is much higher at $L^* = 3.0$ than it is at $L^* = 3.5$.

504 Once we divide the distributions of $D_{\alpha\alpha}$ by activity level, there is no clear trend
 505 for the distributions at $L^* = 2.5$ with increasing geomagnetic activity. The distribu-
 506 tions remain negatively skewed, but the median of the distribution is highest for the sec-
 507 ond highest activity level bin, and lowest for the second lowest activity level bin. At $L^* =$
 508 3.0 , the values of $D_{\alpha\alpha}$ are more ordered; $D_{\alpha\alpha}$ is likely to be higher as activity increases.
 509 At this location, the distribution is not skewed at the lowest activity level, becoming much
 510 more negatively skewed as the activity increases. At $L^* = 3.5$, the distributions of $D_{\alpha\alpha}$
 511 are very similar for all three geomagnetic activity bins where $AE < 150$ nT. The low
 512 geomagnetic activity distributions are negatively skewed. For $AE > 150$ nT, the dis-

513 tribution is positively skewed and the median is much higher than for the other activ-
 514 ity bins. Note that all the different distributions of $D_{\alpha\alpha}$ for different values of geomag-
 515 netic activity overlap considerably, and that the difference between their medians is small
 516 in comparison to their width. We will investigate this further in Section 5.

Figure 8: Coefficient of variation c for all input quantities and $D_{\alpha\alpha}$ for $E = 0.5$ MeV and $\alpha = 30^\circ$. From top to bottom, c values for $D_{\alpha\alpha}$, δB^2 , n_e , f_{pe}/f_{ce} and B_0 . Stars indicate where c has been calculated using equation (2), and circles indicate where c has been calculated using equation (3).

517 The difference in variability between inputs to $D_{\alpha\alpha}$ and the diffusion coefficient it-
 518 self is summarized in Figure 8. The stars indicate values of c calculated using equation
 519 2 for normally-distributed variables, and circles indicate values of c calculated using equa-
 520 tion 3 for log-normally distributed variables. The value of c for $D_{\alpha\alpha}$ at $L^* = 2.5$ is very
 521 large, and is not shown on the plot. It can be argued that equation 3 is an inappropri-
 522 ate description of variance when the underlying distribution is so skewed. The variabil-
 523 ity in all the inputs combines to yield an even larger variability in $D_{\alpha\alpha}$ at energy $E =$
 524 0.5 MeV and $\alpha = 30^\circ$. To understand the source of this variability at a single pitch-
 525 angle, we now consider $D_{\alpha\alpha}(\alpha)$.

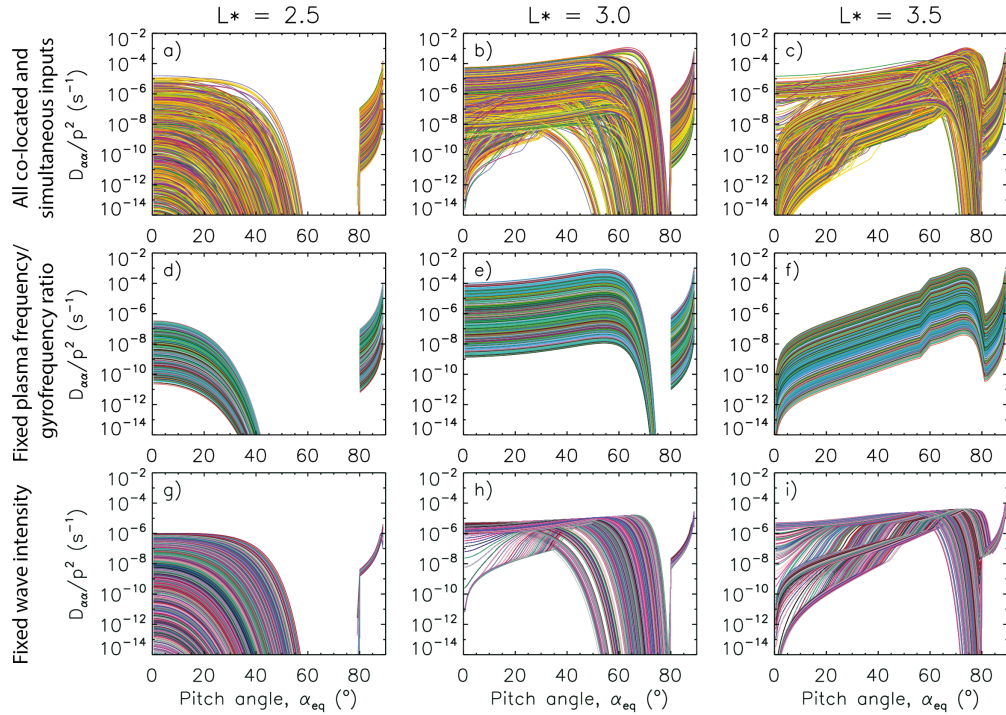


Figure 9: All the $D_{\alpha\alpha}(\alpha)$ for $E = 0.5$ MeV calculated in this study from co-located and simultaneous values of f_{pe}/f_{ce} and δB for (a) $L^* = 3.5$, (b) $L^* = 3.0$ and (c) $L^* = 2.5$. In (d-f), the plasma to gyrofrequency ratio is kept fixed at the average value, and the wave intensity is varied according to the observations. In (g-i), the wave intensity is fixed to the average value and the plasma to gyrofrequency ratio is varied according to the observations.

Figure 9(a-c) shows all the values of $D_{\alpha\alpha}$ calculated using PADIE from co-located and simultaneous observations of f_{pe}/f_{ce} and δB^2 , this time demonstrating the dependence of $D_{\alpha\alpha}$ on α . It is clear that not only the value of $D_{\alpha\alpha}$ changes with the different inputs, but the functional form also varies. Horne et al. (2003b) demonstrate that the shape of $D_{\alpha\alpha}(\alpha)$ depends on the ratio of plasma frequency to gyrofrequency, and our results echo those earlier findings. The apparent independence of the two input parameters (see Figure 6) makes it feasible to investigate the variability of $D_{\alpha\alpha}$ when holding one of the inputs constant, to demonstrate the different ways in which the two input parameters influence the value of $D_{\alpha\alpha}$.

Figure 9(d-f) shows the variability in $D_{\alpha\alpha}$ when f_{pe}/f_{ce} is kept fixed at its mean observed value, and Figure 9(g-i) demonstrates the variability when δB^2 is kept at its mean observed value. Panels (d-f) emphasize that the intensity of the waves changes the size of $D_{\alpha\alpha}$ but not the shape. The variation in the wave intensity therefore affects electrons at all pitch angles equally, behaving like a scaling parameter on the rate of pitch angle diffusion. On the other hand, the number density and magnetic field strength significantly changes the shape and size of $D_{\alpha\alpha}$, as shown by panels (g-i) (note that in Figure 9, the vertical axes span many orders of magnitude). The observed variability in f_{pe}/f_{ce} can result in large changes in the range of resonant pitch-angles for the plasmaspheric hiss. For example, the range of cyclotron resonance at low pitch angles at $L^* = 2.5$ is significantly altered due to the observed variability in f_{pe}/f_{ce} . The range of variability of f_{pe}/f_{ce} likely explains the long negative tail of the distribution of $D_{\alpha\alpha}$ in Figure 7(a) as the resonant energies are controlled by the ratio. Hence variations in the plasma to gyrofrequency ratio alter the pitch angle range over which plasmaspheric hiss can scatter electrons via cyclotron resonances. As such, the pitch angle range that hiss waves can scatter into the loss cone is largely dependent on the value of f_{pe}/f_{ce} , particularly for the $L^* = 2.5$ and $L^* = 3.0$ bins. At $L^* = 2.5$, for some values of f_{pe}/f_{ce} , $D_{\alpha\alpha}$ can be less than 10^{-14} for all $\alpha < 80^\circ$ suggesting that, under these conditions, hiss waves are not an effective loss mechanism for $E = 500$ keV electrons, regardless of the wave intensity. At the lowest range of pitch angles, the variability in the diffusion coefficients is maximized, which means that the potential loss of electrons into the loss-cone by pitch-angle scattering is also highly variable. At higher pitch angles ($> 80^\circ$), where hiss waves scatter electrons via the Landau resonance, variations in f_{pe}/f_{ce} have little effect on the rate of scattering.

In addition to influencing the electron pitch angle range which can be lost from the radiation belt region due to scattering from plasmaspheric hiss, variations in the f_{pe}/f_{ce} ratio will affect electron pitch angle distributions. Cap-top pitch angle distributions (Zhao et al., 2018; Allison et al., 2018) are formed from hiss wave scattering due to the gap in $D_{\alpha\alpha}$ that arises between the cyclotron and Landau resonances (Lyons et al., 1972; Meredith et al., 2009). Figure 9g-i shows that variations in the plasma to gyrofrequency ratio alter the pitch angle range of this $D_{\alpha\alpha}$ gap and, as such, will influence the width of the resulting cap-top of pitch angle distributions. Note that panels d and e show minimal variation in the size of the $D_{\alpha\alpha}$ gap, indicating that varying δB power will have little influence on the form of cap top pitch angle distributions, but instead govern the rate at which this form is reached.

5 Discussion

Most empirical parameterized models of diffusion coefficients (e.g. Subbotin and Shprits (2009); Fok et al. (2011); Glauert et al. (2013); Horne et al. (2013); Tu et al. (2013)) use independent models of magnetic field and number density, and average values of observed wave parameters such as intensity along with an averaged functional dependence of intensity on frequency and wavenormal angle as inputs. In this work, we have instead investigated the range of possible diffusion coefficients obtained when using a large number of co-located and simultaneous measurements of input parameters. The two inputs

578 we have chosen for our demonstration do not have any obvious relationships (see Fig-
 579 ure 6) and so it is reasonable to study the variability of $D_{\alpha\alpha}$ in response to each of the
 580 inputs independently.

Figure 10: A demonstration of the variability in $D_{\alpha\alpha}(E = 0.5\text{MeV}, \alpha = 30^\circ)$ for different methods of calculation: (i) values calculated using the method detailed in Section 7, (ii) a value calculated separately for the mean δB^2 and mean f_{pe}/f_{ce} in each location bin (asterisk), and a value calculated for the median δB^2 and median f_{pe}/f_{ce} (circle), (iii) values calculated using the mean f_{pe}/f_{ce} and all δB^2 values shown in Figure 5, (iv) values calculated using the mean δB^2 , and all f_{pe}/f_{ce} values shown in Figure 4. For each of the cases (i), (iii) and (iv), the median is shown with a circle and upper/lower quartiles are indicated with the bar. Means are indicated with an asterisk.

581 The variability of $D_{\alpha\alpha}$ when calculated in different ways is summarized in Figure
 582 10. For each location bin, we show the mean, median and interquartile range (IQR) when
 583 $D_{\alpha\alpha}$ is calculated using the full distribution of contemporaneous measurements (black),
 584 the full distribution of δB^2 and the mean value of f_{pe}/f_{ce} (red) and the full distribution
 585 of f_{pe}/f_{ce} , but the mean value of δB^2 (magenta). The value of $D_{\alpha\alpha}$ calculated using the
 586 mean values of f_{pe}/f_{ce} and δB^2 is shown with a blue asterisk, and the value of $D_{\alpha\alpha}$ cal-
 587 culated using the median values of f_{pe}/f_{ce} and δB^2 is shown with a blue circle. At all
 588 locations studied, the IQR is largest when the full variability of f_{pe}/f_{ce} and δB^2 is in-
 589 cluded. At $L^* = 2.5$, the plasma to gyrofrequency ratio is responsible for most of the
 590 variability, whereas at the other locations, the wave intensity variability plays a larger
 591 role. Interestingly, for $L^* = 3.5$, changing f_{pe}/f_{ce} leads to a small number of very large
 592 $D_{\alpha\alpha}$ values which skew the mean of the full sample (see the final column of the lowest
 593 panel in Figure 10).

594 While the median values of $D_{\alpha\alpha}$ do not seem very sensitive to the method of combin-
 595 ing the measurements, the mean values of $D_{\alpha\alpha}$ are very sensitive. The underlying dis-
 596 tributions of $D_{\alpha\alpha}$ shown in Figure 7 are log-skew-normal, and so the mean value of the
 597 distribution will be large for such large variances. Hence the mean value of $D_{\alpha\alpha}$ is largest
 598 for the calculation of $D_{\alpha\alpha}$ that yields the largest variance, i.e. when the variability of both
 599 inputs is incorporated. The median value, on the other hand, is affected much less by
 600 changes in the size of the variance of the distributions of $D_{\alpha\alpha}$. For all three L^* bins, the
 601 value of $D_{\alpha\alpha}$ calculated from the means of the input values is much less than the mean
 602 value of $D_{\alpha\alpha}$ calculated from all contemporaneous measurements (i.e. the asterisk in the
 603 first column of Figure 10 is always much larger than the asterisk in the second column).
 604 This suggests that using mean input values to calculate $D_{\alpha\alpha}$ does not capture the high-
 605 est values of $D_{\alpha\alpha}$ at that location, and may indicate why event-specific diffusion coef-
 606 ficients (e.g. those used by Ripoll et al. (2016); Ma et al. (2018)) may yield quite differ-
 607 ent diffusion coefficients to the parameterized models. We note also that at $L^* = 2.5$,
 608 the variability of the ratio f_{pe}/f_{ce} appears to be responsible for most of the variability
 609 in $D_{\alpha\alpha}$ (see Figure 10), and yet the variability of f_{pe}/f_{ce} at $L^* = 2.5$ as measured by
 610 the coefficient of variation (Figure 8) is similar to that at all location bins studied in this
 611 analysis. The sensitivity of the diffusion coefficient to different input parameters also ap-
 612 pears to vary from one location to another.

613 The results shown in the paper indicate that that effects of combining co-located
 614 and simultaneous measurements of the inputs for the diffusion coefficient calculation is
 615 to increase the variability of the resulting diffusion coefficients above the variability of
 616 the independent inputs (see Figure 10). Note that in this analysis, there is no obvious
 617 relationship between the variability, or underlying distribution, of the inputs, and the
 618 variability and underlying distribution of the diffusion coefficients, just that the variabil-

619 ity increases when the inputs are combined. The effects of variability in other inputs,
 620 such as wavenormal angle (Hartley et al., 2018), and wave frequency range (Li et al., 2015),
 621 should also be included in a future analysis. Indeed, the variability of plasma compo-
 622 sition (Jahn et al., 2017) may also play a major role.

623 It is important to reiterate that the large values of variance in our diffusion coef-
 624 ficients result not just from the variability of the inputs (i.e. from the variability in plasma
 625 conditions and wave characteristics), but from the sensitivity of the calculation of the
 626 diffusion coefficients to those inputs. It is also important to note that the diffusion co-
 627 efficients presented in this paper are for a single value of energy. When the plasma to
 628 gyrofrequency ratio is changed, the wave-particle resonance tends to move in energy-space;
 629 effectively, if diffusion is decreased at one energy due to changes in f_{pe}/f_{ce} , then it can
 630 be increased at another. Hence the variability in the diffusion coefficients at a single en-
 631 ergy is not the full picture of phase space diffusion due to waves at a particular location,
 632 and the effects of the variability in $D_{\alpha\alpha}(E, \alpha)$ across all energies and pitch-angles should
 633 be investigated using numerical experiments. That is the natural next step for this work.

634 We do not yet know how the variability of diffusion coefficients presented here af-
 635 fects the modelling of diffusion processes in the outer radiation belt. The large values
 636 of variance in our diffusion coefficients indicate that a probabilistic model is worth pur-
 637 suing to capture the physics of wave-particle interactions in the radiation belts. A stochas-
 638 tic parameterization is ideal to capture variable processes in physics-based models that
 639 incorporate empirical parameterization. The use of stochastic parameterizations in other
 640 branches of Earth Science (e.g. Berner et al. (2017); Pulido, Tandeo, Bocquet, Carrasi,
 641 and Lucini (2018)) demonstrates significant improvement over deterministic parameter-
 642 izations for a range of different processes. The results presented in this paper provide
 643 the underlying distribution of the diffusion coefficients, and the size of the variance, for
 644 three different locations and provide some of the necessary information to test differences
 645 between deterministic and stochastic parameterization. A natural next step for this re-
 646 search is to perform the numerical experiments necessary to investigate whether descrip-
 647 tions that capture the variability of the diffusion coefficients provide different diffusion
 648 model evolution than their deterministic counterparts.

649 Until now, models of diffusion coefficients used in radiation belts models have in-
 650 corporated temporal variability in drift- and bounce-averaged $D_{\alpha\alpha}$ by parameterizing
 651 the inputs for the diffusion coefficients (largely the wave parameters) by geomagnetic ac-
 652 tivity indices such as AE (e.g. Horne et al. (2013); Meredith et al. (2018)) or Kp (e.g.
 653 Albert et al. (2009); Ozeke et al. (2014); Glauert et al. (2018)). Here we discuss how well
 654 AE parameterizes the $D_{\alpha\alpha}$ by using a quantitative measure otherwise known as the sep-
 655 aration proxy (Bentley et al., 2018b). There are a number of ways to describe the over-
 656 lap between different bins of observations, but we will use this simple metric because the
 657 standard deviation of $\log(D_{\alpha\alpha})$ is relatively constant over all the geomagnetic activity
 658 bins shown in Figure 7(d-f). We use the signed ratio of the difference in mean values be-
 659 tween adjacent geomagnetic activity bins to the standard deviation. Specifically, for two
 660 neighboring bins $b_i; b_{i+1}$, we define

$$661 \quad \chi_S = \frac{(\mu_{i+1} - \mu_i)}{\frac{1}{2}(\sigma_i + \sigma_{i+1})} \quad (4)$$

662 where μ is the mean and σ_i the standard deviation of $\log(D_{\alpha\alpha})$. Note that in Bentley
 663 et al. (2018b), the quantity χ_S is unsigned, i.e. χ_S depends only on the absolute size of
 664 the difference between the means of neighboring bins. However, for our purposes, we note
 665 that a signed quantity retains valuable information, since an increase in geomagnetic ac-
 666 tivity does not necessarily guarantee an increase in the mean of $\log(D_{\alpha\alpha})$. The quan-
 667 tity χ_S is very similar to Cohen's d (Cohen, 1988), and much of the same interpretation
 668 can be used here (see Bentley et al. (2018b) for a discussion of why χ_S is preferable in

Table 2: Signed separation proxy χ_S for distributions of $D_{\alpha\alpha}$ for $E = 0.5$ MeV and $\alpha = 30^\circ$ binned by geomagnetic activity in each location bin.

	$L^* = 2.5$	$L^* = 3.0$	$L^* = 3.5$
$AE < 50$ nT and $50 < AE < 100$ nT	-0.5	0.1	0.4
$50 < AE < 100$ nT and $100 < AE < 150$ nT	0.6	0.5	0.1
$100 < AE < 150$ nT and $AE > 150$ nT	-0.4	0.5	1.1

our case). When $\chi_S = 0$, the two distributions completely overlap, and when $\chi_S = 1$, the point of overlap between the two distributions is exactly one standard deviation from either mean, i.e. if both distributions were normal, then only 16% of data from each distribution would overlap when $\chi_S = 1$. Essentially, a larger value of χ_S indicates a "better" parameterization than a lower value, since highly overlapping distributions would indicate that our chosen parameter did not describe the diffusion coefficients well.

Table 2 shows the values of χ_S for the distributions of $\log(D_{\alpha\alpha})$ shown in Figure 7(d-f). At $L^* = 2.5$, increasing geomagnetic activity does not correspond to an increase in the mean value of $\log(D_{\alpha\alpha})$; the distributions jump around considerably as geomagnetic activity is increased. The expected increasing trends are seen at $L^* = 3.0$ and $L^* = 3.5$, with positive χ_S throughout, although there is significant overlap for some of the lower activity bins. We conclude that although increasing geomagnetic activity describes increasing values of $D_{\alpha\alpha}$ in some locations, this is not universal. An interesting feature of the distributions shown in Figure 7 is that for $L^* = 3.0$ and $L^* = 3.5$ there is evidence of a thresholding effect, rather than a steady increase in diffusion with geomagnetic activity. For $L^* = 3.0$, there is a large shift in the distribution towards the right between the $50 < AE < 100$ nT bin and the $100 < AE < 150$ nT bin. For $L^* = 3.5$, this large shift towards higher values of diffusion occurs between the $100 < AE < 150$ nT bin and the $1AE > 150$ nT bin. Of course, our small location bins have necessitated coarse-graining in geomagnetic activity space in order to preserve sufficient data to study the distributions of $D_{\alpha\alpha}$. Future analyses will consider larger volume bins (perhaps by including larger ranges in MLT or magnetic latitude) so that we have sufficient data coverage to study higher geomagnetic activity conditions in more detail and investigate the dependence of the diffusion coefficients on higher (and much rarer) values of geomagnetic activity.

6 Conclusions

In this study we determine the range of values of $D_{\alpha\alpha}$ due to plasmaspheric hiss as a result of realistic variations in two key input parameters. We chose three locations in the magnetic equatorial plane in the inner magnetosphere, all at $9 < \text{MLT} < 10$: $L^* = 2.5$, $L^* = 3.0$, and $L^* = 3.5$. The results from this study suggest that the diffusion coefficients calculated from co-located and simultaneous observations of plasma and wave properties exhibit large variability, and a highly non-Gaussian distribution. The input parameters to the diffusion coefficient calculation vary in different ways: the plasma frequency to gyrofrequency ratio is close to normally-distributed with a small variance, and the wave intensities are log-skew normally-distributed with a large variance. The extent of the variation in $D_{\alpha\alpha}$ varies in each of the three different locations we studied. As previous work suggests, variations in the wave intensity affects $D_{\alpha\alpha}$ at all pitch-angles, behaving like a scaling parameter for the diffusion coefficients. Variations in the plasma to gyrofrequency ratio change how effectively the plasmaspheric hiss interacts with electrons via cyclotron resonance and can radically alter the $D_{\alpha\alpha}(\alpha)$ profile at a constant

energy. For $L^* = 2.5$, the variations are largely due to changing plasma to gyrofrequency ratio, even though the variation in frequency ratio was very similar for the three locations studied. We conclude that the sensitivity of $D_{\alpha\alpha}$ can also be location-specific. For the $L^* = 3.0$ and $L^* = 3.5$ bins, the variations in $D_{\alpha\alpha}$ were primarily due to the wave intensity variations. However, for $L^* = 3.5$, changing frequency ratio leads to a small number of large $D_{\alpha\alpha}$ values which skews the mean of the full sample.

We suggest that it is important to capture the variability of the diffusion coefficients because these parameterizations are the key expression of sub-grid physics used in large-scale radiation belt diffusion models. We have seen that the variability of separate inputs combines to give increased variability in the calculated diffusion coefficients, not least because the quasilinear diffusion coefficients are not simple functions of the inputs. Note that we do not consider all sources of variability in this work, and that other important parameters, such as the variability of plasma composition and wave intensity as a function of frequency and wavenormal angle should also be investigated. The effect of the large variability in diffusion coefficients is currently unknown, and future work is planned to investigate the behaviour of diffusion models that include this variability. For example, knowledge of the variability of the diffusion coefficients can be used to great advantage in a stochastic parameterization of diffusion and this investigation is the first step towards a model that includes the full variability of wave-particle interactions possible in the radiation belts.

Acknowledgments

This research was supported by STFC grant ST/R000921/1, as well as the Natural Environment Research Council (NERC) Highlight Topic Grant NE/P01738X/1 (Rad-Sat BAS), NE/P017274/1 (Rad-Sat UoR), and NE/P017185/1 (Rad-Sat MSSL). HJA was supported by NERC Doctoral Training Programme NE/L002507/1 and RLT was supported by the Engineering and Physical Sciences Research Council (EPSRC) grant EP/L016613/1.

We acknowledge the NASA Van Allen Probes and Craig Kletzing for use of EMFISIS data. The EMFISIS data is available from <https://emfisis.physics.uiowa.edu/data/index>. Diffusion coefficient data displayed in this paper are available at <http://dx.doi.org/10.17864/1947.212>.

References

- Agapitov, O., Artemyev, A., Krasnoselskikh, V., Khotyaintsev, Y. V., Mourenas, D., Breuillard, H., ... Rolland, G. (2013). Statistics of whistler mode waves in the outer radiation belt: Cluster staff-sa measurements. *Journal of Geophysical Research: Space Physics*, *118*(6), 3407-3420. doi: 10.1002/jgra.50312
- Albert, J. M., Meredith, N. P., & Horne, R. B. (2009). Three-dimensional diffusion simulation of outer radiation belt electrons during the 9 October 1990 magnetic storm. *Journal of Geophysical Research: Space Physics*, *114*(A9). doi: 10.1029/2009JA014336
- Albert, J. M., Starks, M. J., Horne, R. B., Meredith, N. P., & Glauert, S. A. (2016). Quasi-linear simulations of inner radiation belt electron pitch angle and energy distributions. *Geophysical Research Letters*, *43*(6), 2381-2388. doi: 10.1002/2016GL067938
- Allison, H. J., Horne, R. B., Glauert, S. A., & Del Zanna, G. (2018). Determination of the equatorial electron differential flux from observations at low earth orbit. *Journal of Geophysical Research: Space Physics*. doi: 10.1029/2018ja025786
- Bentley, S. N., Watt, C. E. J., Owens, M. J., & Rae, I. J. (2018a). Ulf wave activity in the magnetosphere: Resolving solar wind interdependencies to identify driving mechanisms. *Journal of Geophysical Research: Space Physics*, *123*(4), 2745-2771. doi: 10.1002/2017JA024740
- Bentley, S. N., Watt, C. E. J., Rae, I. J., Owens, M. J., Murphy, K. R., Lockwood,

- 759 M., & Sandhu, J. K. (2018b). Capturing uncertainty in magnetospheric
760 ultra-low frequency wave models. *Space Weather, under review*.
- 761 Berner, J., Achatz, U., Batt, L., Bengtsson, L., Cmara, A. d. l., Christensen, H. M.,
762 ... Yano, J.-I. (2017). Stochastic parameterization: Toward a new view of
763 weather and climate models. *Bulletin of the American Meteorological Society*,
764 *98*(3), 565-588. doi: 10.1175/BAMS-D-15-00268.1
- 765 Blum, L. W., Halford, A., Millan, R., Bonnell, J. W., Goldstein, J., Usanova, M., ...
766 Li, X. (2015). Observations of coincident EMIC wave activity and duskside
767 energetic electron precipitation on 1819 January 2013. *Geophysical Research*
768 *Letters*, *42*(14), 5727-5735. doi: 10.1002/2015GL065245
- 769 Chen, L., Li, W., Bortnik, J., & Thorne, R. M. (2012). Amplification of whistler-
770 mode hiss inside the plasmasphere. *Geophysical Research Letters*, *39*(8). doi:
771 10.1029/2012GL051488
- 772 Cohen, J. (1988). *Statistical power analysis for the behavioral sciences*. Lawrence
773 Erlbaum Associates.
- 774 Drozdov, A. Y., Shprits, Y. Y., Usanova, M. E., Aseev, N. A., Kellerman, A. C.,
775 & Zhu, H. (2017). EMIC wave parameterization in the long-term VERB
776 code simulation. *Journal of Geophysical Research: Space Physics*, *122*(8),
777 8488-8501. doi: 10.1002/2017JA024389
- 778 Fei, Y., Chan, A. A., Elkington, S. R., & Wiltberger, M. J. (2006). Radial diffusion
779 and mhd particle simulations of relativistic electron transport by ulf waves in
780 the september 1998 storm. *Journal of Geophysical Research: Space Physics*,
781 *111*(A12). doi: 10.1029/2005JA011211
- 782 Fok, M.-C., Glocer, A., Zheng, Q., Horne, R., Meredith, N., Albert, J., & Nagai, T.
783 (2011). Recent developments in the radiation belt environment model. *Jour-*
784 *nal of Atmospheric and Solar-Terrestrial Physics*, *73*(11), 1435 – 1443. doi:
785 10.1016/j.jastp.2010.09.033
- 786 Glauert, S. A., & Horne, R. B. (2005). Calculation of pitch angle and energy dif-
787 fusion coefficients with the padie code. *Journal of Geophysical Research: Space*
788 *Physics*, *110*(A4). doi: 10.1029/2004JA010851
- 789 Glauert, S. A., Horne, R. B., & Meredith, N. P. (2013). Three-dimensional elec-
790 tron radiation belt simulations using the BAS Radiation Belt Model with
791 new diffusion models for chorus, plasmaspheric hiss, and lightning-generated
792 whistlers. *Journal of Geophysical Research: Space Physics*, *119*(1), 268-289.
793 doi: 10.1002/2013JA019281
- 794 Glauert, S. A., Horne, R. B., & Meredith, N. P. (2014a). Three-dimensional elec-
795 tron radiation belt simulations using the BAS Radiation Belt Model with
796 new diffusion models for chorus, plasmaspheric hiss, and lightning-generated
797 whistlers. *Journal of Geophysical Research: Space Physics*, *119*(1), 268-289.
798 doi: 10.1002/2013JA019281
- 799 Glauert, S. A., Horne, R. B., & Meredith, N. P. (2018). A 30-year simula-
800 tion of the outer electron radiation belt. *Space Weather*, *0*(0). doi:
801 10.1029/2018SW001981
- 802 Hartley, D. P., Kletzing, C. A., Santolk, O., Chen, L., & Horne, R. B. (2018). Statis-
803 tical properties of plasmaspheric hiss from van allen probes observations. *Jour-*
804 *nal of Geophysical Research: Space Physics*, *123*(4), 2605-2619. doi: 10.1002/
805 2017JA024593
- 806 Horne, R. B., Glauert, S. A., & Thorne, R. M. (2003b). Resonant diffusion of radi-
807 ation belt electrons by whistler-mode chorus. *Geophysical Research Letters*, *30*,
808 1493-1496.
- 809 Horne, R. B., Kersten, T., Glauert, S. A., Meredith, N. P., Boscher, D., Sicard-Piet,
810 A., ... Li, W. (2013). A new diffusion matrix for whistler mode chorus waves.
811 *Journal of Geophysical Research: Space Physics*, *118*(10), 6302-6318. doi:
812 10.1002/jgra.50594
- 813 Horne, R. B., Meredith, N. M., Glauert, S. A., & Kersten, T. (2016). Wave driven

- 814 diffusion in radiation belt dynamics. In G. Balasis, I. A. Daglis, & I. R. Mann
815 (Eds.), *Waves, particles, and storms in geospace: a complex interplay* (p. 217-
816 243). Oxford: Oxford University Press.
- 817 Horne, R. B., Thorne, R. M., Glauert, S. A., Albert, J. M., Meredith, N. P., & An-
818 derson, R. R. (2005a). Timescale for radiation belt electron acceleration by
819 whistler mode chorus waves. *Journal of Geophysical Research: Space Physics*,
820 *110*(A3). doi: 10.1029/2004JA010811
- 821 Horne, R. B., Thorne, R. M., Shprits, Y. Y., Meredith, N. M., Glauert, S. A., Smith,
822 A. J., ... Decreau, P. M. E. (2005b). Wave acceleration of electrons in the
823 Van Allen radiation belts. *Nature*, *437*. doi: 10.1038/nature03939
- 824 Jahn, J.-M., Goldstein, J., Reeves, G. D., Fernandes, P. A., Skoug, R. M., Larsen,
825 B. A., & Spence, H. E. (2017). The warm plasma composition in the inner
826 magnetosphere during 20122015. *Journal of Geophysical Research: Space*
827 *Physics*, *122*(11), 11,018-11,043. doi: 10.1002/2017JA024183
- 828 Kellerman, A. C., & Shprits, Y. Y. (2012). On the influence of solar wind conditions
829 on the outer-electron radiation belt. *Journal of Geophysical Research: Space*
830 *Physics*, *117*(A5). doi: 10.1029/2011JA017253
- 831 Kersten, T., Horne, R. B., Glauert, S. A., Meredith, N. P., Fraser, B. J., & Grew,
832 R. S. (2014). Electron losses from the radiation belts caused by EMIC waves.
833 *Journal of Geophysical Research: Space Physics*, *119*(11), 8820-8837. doi:
834 10.1002/2014JA020366
- 835 Kim, K.-C., Shprits, Y., Subbotin, D., & Ni, B. (2011). Understanding the dynamic
836 evolution of the relativistic electron slot region including radial and pitch angle
837 diffusion. *Journal of Geophysical Research: Space Physics*, *116*(A10).
- 838 Kletzing, C. A., Kurth, W. S., Acuna, M., MacDowall, R. J., Torbert, R. B.,
839 Averkamp, T., ... Tyler, J. (2013, Nov 01). The electric and magnetic
840 field instrument suite and integrated science (emfisis) on rbsp. *Space Sci-*
841 *ence Reviews*, *179*(1), 127-181. Retrieved from [https://doi.org/10.1007/](https://doi.org/10.1007/s11214-013-9993-6)
842 [s11214-013-9993-6](https://doi.org/10.1007/s11214-013-9993-6) doi: 10.1007/s11214-013-9993-6
- 843 Koons, H. C., & Roeder, J. L. (1990, October). A survey of equatorial magneto-
844 spheric wave activity between 5 and 8 R_E . *Planetary and Space Science*, *38*,
845 1335-1341. doi: 10.1016/0032-0633(90)90136-E
- 846 Kurth, W. S., De Pascuale, S., Faden, J. B., Kletzing, C. A., Hospodarsky, G. B.,
847 Thaller, S., & Wygant, J. R. (2015). Electron densities inferred from
848 plasma wave spectra obtained by the waves instrument on van allen probes.
849 *Journal of Geophysical Research: Space Physics*, *120*(2), 904-914. doi:
850 10.1002/2014JA020857
- 851 Lam, M. M., Horne, R. B., Meredith, N. P., & Glauert, S. A. (2007). Modeling
852 the effects of radial diffusion and plasmaspheric hiss on outer radiation belt
853 electrons. *Geophysical Research Letters*, *34*(20). doi: 10.1029/2007GL031598
- 854 Lejosne, S., Boscher, D., Maget, V., & Rolland, G. (2012). Bounce-averaged ap-
855 proach to radial diffusion modeling: From a new derivation of the instanta-
856 neous rate of change of the third adiabatic invariant to the characterization of
857 the radial diffusion process. *Journal of Geophysical Research: Space Physics*,
858 *117*(A8). doi: 10.1029/2012JA018011
- 859 Li, W., Ma, Q., Thorne, R. M., Bortnik, J., Kletzing, C. A., Kurth, W. S., ...
860 Nishimura, Y. (2015). Statistical properties of plasmaspheric hiss derived
861 from Van Allen Probes data and their effects on radiation belt electron dynam-
862 ics. *Journal of Geophysical Research: Space Physics*, *120*(5), 3393-3405. doi:
863 10.1002/2015JA021048
- 864 Li, W., Thorne, R. M., Bortnik, J., Tao, X., & Angelopoulos, V. (2012). Charac-
865 teristics of hiss-like and discrete whistler-mode emissions. *Geophysical Research*
866 *Letters*, *39*(18). doi: 10.1029/2012GL053206
- 867 Lyons, L. R., Thorne, R. M., & Kennel, C. F. (1972). Pitch-angle diffusion of radi-
868 ation belt electrons within the plasmasphere. *Journal of Geophysical Research*,

- 869 77(19), 3455-3474. doi: 10.1029/JA077i019p03455
- 870 Ma, Q., Li, W., Bortnik, J., Thorne, R. M., Chu, X., Ozeke, L. G., ... Claudepierre,
871 S. G. (2018). Quantitative evaluation of radial diffusion and local acceleration
872 processes during geomagnetic challenge events. *Journal of Geophysical Research: Space*
873 *Physics*, 123(3), 1938-1952. doi: 10.1002/2017JA025114
- 874 Ma, Q., Li, W., Thorne, R. M., Ni, B., Kletzing, C. A., Kurth, W. S., ... An-
875 gelopoulos, V. (2015). Modeling inward diffusion and slow decay of energetic
876 electrons in the earth's outer radiation belt. *Geophysical Research Letters*,
877 42(4), 987-995. doi: 10.1002/2014GL062977
- 878 Malaspina, D. M., Jaynes, A. N., Hospodarsky, G., Bortnik, J., Ergun, R. E., &
879 Wygant, J. (2017). Statistical properties of low-frequency plasmaspheric
880 hiss. *Journal of Geophysical Research: Space Physics*, 122(8), 8340-8352. doi:
881 10.1002/2017JA024328
- 882 Malaspina, D. M., Ripoll, J.-F., Chu, X., Hospodarsky, G., & Wygant, J. (2018).
883 Variation in plasmaspheric hiss wave power with plasma density. *Geophysical*
884 *Research Letters*, 45(18), 9417-9426. doi: 10.1029/2018GL078564
- 885 Mann, I. R., Ozeke, L. G., Murphy, K. R., Claudepierre, S. G., Turner, D. L., Baker,
886 D. N., ... Honary, F. (2016). Explaining the dynamics of the ultra-relativistic
887 third Van Allen radiation belt. *Nature Physics*, 12, 978-983.
- 888 Meredith, N. P., Horne, R. B., & Anderson, R. R. (2001). Substorm dependence
889 of chorus amplitudes: Implications for the acceleration of electrons to rela-
890 tivistic energies. *Journal of Geophysical Research: Space Physics*, 106(A7),
891 13165-13178. doi: 10.1029/2000JA900156
- 892 Meredith, N. P., Horne, R. B., Glauert, S. A., & Anderson, R. R. (2007). Slot re-
893 gion electron loss timescales due to plasmaspheric hiss and lightning-generated
894 whistlers. *Journal of Geophysical Research: Space Physics*, 112(A8). doi:
895 10.1029/2007JA012413
- 896 Meredith, N. P., Horne, R. B., Glauert, S. A., Baker, D. N., Kanekal, S. G., &
897 Albert, J. M. (2009). Relativistic electron loss timescales in the slot re-
898 gion. *Journal of Geophysical Research: Space Physics*, 114(A3). doi:
899 10.1029/2008JA013889
- 900 Meredith, N. P., Horne, R. B., Glauert, S. A., Thorne, R. M., Summers, D., Albert,
901 J. M., & Anderson, R. R. (2006). Energetic outer zone electron loss timescales
902 during low geomagnetic activity. *Journal of Geophysical Research: Space*
903 *Physics*, 111(A05212). doi: 10.1029/2005JA011516
- 904 Meredith, N. P., Horne, R. B., Kersten, T., Li, W., Bortnik, J., Sicard, A., &
905 Yearby, K. H. (2018). Global model of plasmaspheric hiss from multiple
906 satellite observations. *Journal of Geophysical Research: Space Physics*, 123(6),
907 4526-4541. doi: 10.1029/2018JA025226
- 908 Meredith, N. P., Horne, R. B., Thorne, R. M., Summers, D., & Anderson, R. R.
909 (2004). Substorm dependence of plasmaspheric hiss. *Journal of Geophysical*
910 *Research: Space Physics*, 109(A6). doi: 10.1029/2004JA010387
- 911 Miyoshi, Y. S., Jordanova, V. K., Morioka, A., & Evans, D. S. (2005). Solar cycle
912 variations of the electron radiation belts: Observations and radial diffusion
913 simulation. *Space Weather*, 2(10). doi: 10.1029/2004SW000070
- 914 Murphy, K. R., Inglis, A. R., Sibeck, D. G., Rae, I. J., Watt, C. E. J., Silveira, M.,
915 ... Nakamura, R. (2018). Determining the mode, frequency, and azimuthal
916 wave number of ULF waves during a HSS and moderate geomagnetic storm.
917 *Journal of Geophysical Research: Space Physics*, 123(8), 6457-6477. doi:
918 10.1029/2017JA024877
- 919 Ni, B., Bortnik, J., Thorne, R. M., Ma, Q., & Chen, L. (2013). Resonant scattering
920 and resultant pitch angle evolution of relativistic electrons by plasmaspheric
921 hiss. *Journal of Geophysical Research: Space Physics*, 118(12), 7740-7751. doi:
922 10.1002/2013JA019260
- 923 Ni, B., Li, W., Thorne, R. M., Bortnik, J., Ma, Q., Chen, L., ... Claudepierre,

- 924 S. G. (2014). Resonant scattering of energetic electrons by unusual low-
 925 frequency hiss. *Geophysical Research Letters*, *41*(6), 1854-1861. doi:
 926 10.1002/2014GL059389
- 927 Ni, B., Thorne, R. M., Shprits, Y. Y., & Bortnik, J. (2008). Resonant scatter-
 928 ing of plasma sheet electrons by whistler-mode chorus: Contribution to
 929 diffuse auroral precipitation. *Geophysical Research Letters*, *35*(11). doi:
 930 10.1029/2008GL034032
- 931 Olson, W. P., & Pfizer, K. (1977). *Magnetospheric magnetic field modelling annual*
 932 *scientific report* (Tech. Rep. No. AFOSR Contract No. F44620-75-c-0033).
- 933 Ozeke, L. G., Mann, I. R., Murphy, K. R., Rae, I. J., & Milling, D. K. (2014). Ana-
 934 lytic expressions for ULF wave radiation belt radial diffusion coefficients. *Jour-*
 935 *nal of Geophysical Research: Space Physics*, *119*(3), 1587-1605. doi: 10.1002/
 936 2013JA019204
- 937 Pulido, M., Tandeo, P., Bocquet, M., Carrassi, A., & Lucini, M. (2018). Stochastic
 938 parameterization identification using ensemble kalman filtering combined with
 939 maximum likelihood methods. *Tellus A: Dynamic Meteorology and Oceanogra-*
 940 *phy*, *70*(1), 1442099. doi: 10.1080/16000870.2018.1442099
- 941 Reeves, G. D., Chen, Y., Cunningham, G. S., Friedel, R. W. H., Henderson,
 942 M. G., Jordanova, V. K., ... Zaharia, S. (2012). Dynamic Radiation En-
 943 vironment Assimilation Model: DREAM. *Space Weather*, *10*(3). doi:
 944 10.1029/2011SW000729
- 945 Ripoll, J.-F., Reeves, G. D., Cunningham, G. S., Loridan, V., Denton, M., Santolk,
 946 O., ... Ukhorskiy, A. Y. (2016). Reproducing the observed energy-dependent
 947 structure of Earth's electron radiation belts during storm recovery with an
 948 event-specific diffusion model. *Geophysical Research Letters*, *43*(11), 5616-
 949 5625. doi: 10.1002/2016GL068869
- 950 Ripoll, J.-F., Santolk, O., Reeves, G. D., Kurth, W. S., Denton, M. H., Loridan,
 951 V., ... Turner, D. L. (2017). Effects of whistler mode hiss waves in March
 952 2013. *Journal of Geophysical Research: Space Physics*, *122*(7), 7433-7462. doi:
 953 10.1002/2017JA024139
- 954 Russell, C. T., Holzer, R. E., & Smith, E. J. (1970). Ogo 3 observations of elf noise
 955 in the magnetosphere: 2. the nature of the equatorial noise. *Journal of Geo-*
 956 *physical Research*, *75*(4), 755-768. doi: 10.1029/JA075i004p00755
- 957 Santolík, O., Němec, F., Gereová, K., Macúšová, E., de Conchy, Y., & Cornilleau-
 958 Wehrlin, N. (2004). Systematic analysis of equatorial noise below the
 959 lower hybrid frequency. *Annales Geophysicae*, *22*(7), 2587-2595. Re-
 960 trieved from <https://www.ann-geophys.net/22/2587/2004/>
 961 10.5194/angeo-22-2587-2004 doi:
 962 10.1029/2002GL016178
- 963 Santolk, O., & Gurnett, D. A. (2003a). Transverse dimensions of chorus in
 964 the source region. *Geophysical Research Letters*, *30*(2). doi: 10.1029/
 965 2002GL016178
- 966 Santolk, O., Gurnett, D. A., Pickett, J. S., Parrot, M., & Cornilleau-Wehrlin, N.
 967 (2003b). Spatio-temporal structure of storm-time chorus. *Journal of Geophysi-*
 968 *cal Research: Space Physics*, *108*(A7). doi: 10.1029/2002JA009791
- 969 Sheeley, B. W., Moldwin, M. B., Rassoul, H. K., & Anderson, R. R. (2001). An
 970 empirical plasmasphere and trough density model: Crres observations. *Journal*
 971 *of Geophysical Research: Space Physics*, *106*(A11), 25631-25641. doi: 10.1029/
 972 2000JA000286
- 973 Spasojevic, M., Shprits, Y. Y., & Orlova, K. (2015). Global empirical models of
 974 plasmaspheric hiss using Van Allen Probes. *Journal of Geophysical Research:*
 975 *Space Physics*, *120*(12), 10,370-10,383. doi: 10.1002/2015JA021803
- 976 Subbotin, D. A., & Shprits, Y. Y. (2009). Three-dimensional modeling of the ra-
 977 diation belts using the Versatile Electron Radiation Belt (VERB) code. *Space*
 978 *Weather*, *7*(10). doi: 10.1029/2008SW000452
- 979 Summers, D., Ni, B., Meredith, N. P., Horne, R. B., Thorne, R. M., Moldwin, M. B.,

- 979 & Anderson, R. R. (2008). Electron scattering by whistler-mode elf hiss
 980 in plasmaspheric plumes. *Journal of Geophysical Research: Space Physics*,
 981 *113*(A4). doi: 10.1029/2007JA012678
- 982 Thompson, R. L., Watt, C. E. J., & Williams, P. D. (2018). Exploring the impacts
 983 of variability in the radial diffusion problem. *Journal of Geophysical Research:*
 984 *Space Physics, under review.*
- 985 Thorne, R. M. (2010). Radiation belt dynamics: The importance of wave-particle in-
 986 teractions. *Geophysical Research Letters*, *37*(22). doi: 10.1029/2010GL044990
- 987 Thorne, R. M., Smith, E. J., Burton, R. K., & Holzer, R. E. (1973). Plasma-
 988 spheric hiss. *Journal of Geophysical Research*, *78*(10), 1581-1596. doi:
 989 10.1029/JA078i010p01581
- 990 Tsurutani, B. T., & Smith, E. J. (1977). Two types of magnetospheric ELF chorus
 991 and their substorm dependences. *Journal of Geophysical Research*, *82*(32),
 992 5112-5128. Retrieved from [https://agupubs.onlinelibrary.wiley.com/](https://agupubs.onlinelibrary.wiley.com/doi/abs/10.1029/JA082i032p05112)
 993 [doi/abs/10.1029/JA082i032p05112](https://agupubs.onlinelibrary.wiley.com/doi/abs/10.1029/JA082i032p05112) doi: 10.1029/JA082i032p05112
- 994 Tu, W., Cunningham, G. S., Chen, Y., Henderson, M. G., Camporeale, E., &
 995 Reeves, G. D. (2013). Modeling radiation belt electron dynamics during gem
 996 challenge intervals with the dream3d diffusion model. *Journal of Geophysical*
 997 *Research: Space Physics*, *118*(10), 6197-6211. doi: 10.1002/jgra.50560
- 998 Tu, W., Cunningham, G. S., Chen, Y., Morley, S. K., Reeves, G. D., Blake, J. B., ...
 999 Spence, H. (2014). Event-specific chorus wave and electron seed population
 1000 models in dream3d using the van allen probes. *Geophysical Research Letters*,
 1001 *41*(5), 1359-1366. doi: 10.1002/2013GL058819
- 1002 Varotsou, A., Boscher, D., Bourdarie, S., Horne, R. B., Glauert, S. A., & Meredith,
 1003 N. P. (2008). Simulation of the outer radiation belt electrons near geosyn-
 1004 chronous orbit including both radial diffusion and resonant interaction with
 1005 whistler-mode chorus waves. *Geophysical Research Letters*, *32*(19). doi:
 1006 10.1029/2005GL023282
- 1007 Watt, C. E. J., Rae, I. J., Murphy, K. R., Anekallu, C., Bentley, S. N., & Forsyth, C.
 1008 (2017). The parameterization of wave-particle interactions in the Outer Radia-
 1009 tion Belt. *Journal of Geophysical Research: Space Physics*, *122*(9), 9545-9551.
 1010 doi: 10.1002/2017JA024339
- 1011 Zhao, H., Friedel, R. H. W., Chen, Y., Reeves, G. D., Baker, D. N., Li, X., ...
 1012 Spence, H. E. (2018). An empirical model of radiation belt electron pitch angle
 1013 distributions based on van allen probes measurements. *Journal of Geophysical*
 1014 *Research: Space Physics*, *123*(5), 3493-3511. doi: 10.1029/2018JA025277

Figure 1.

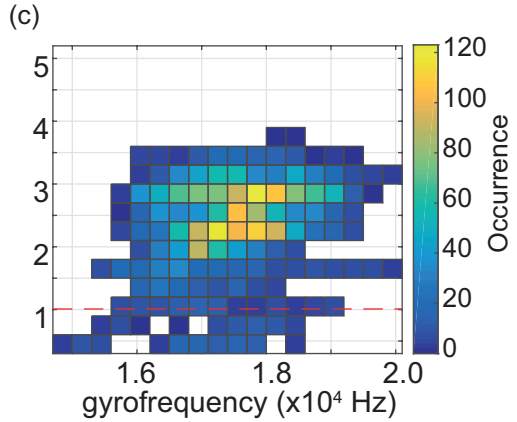
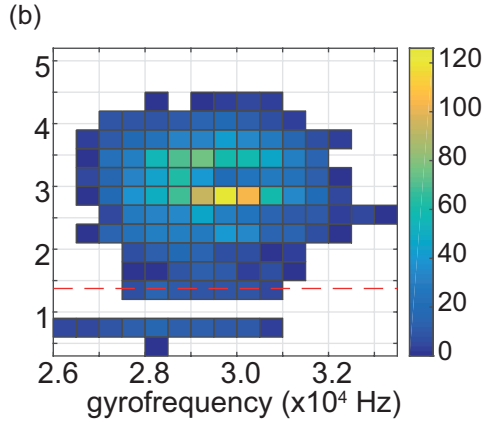
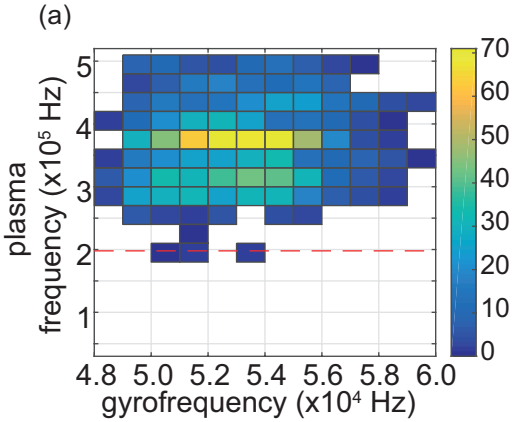
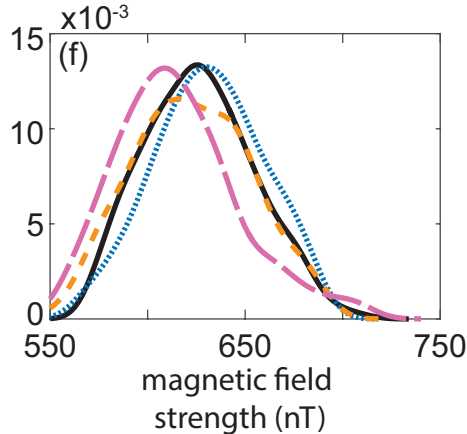
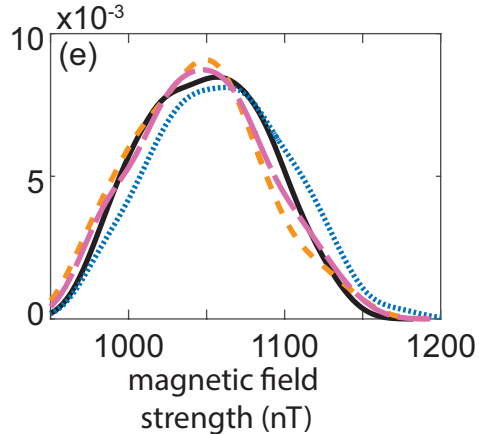
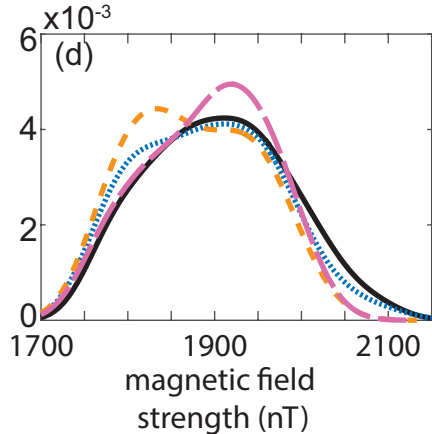
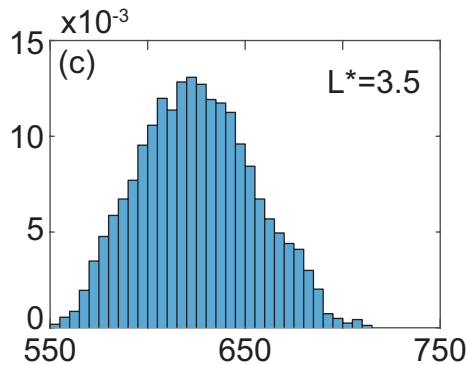
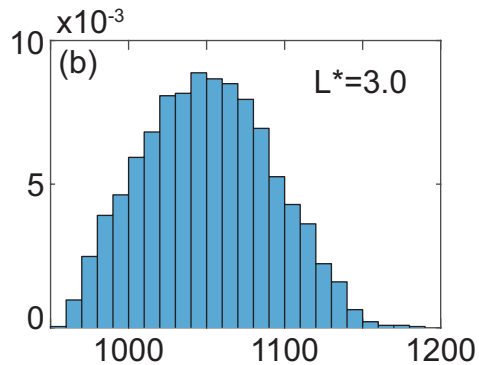
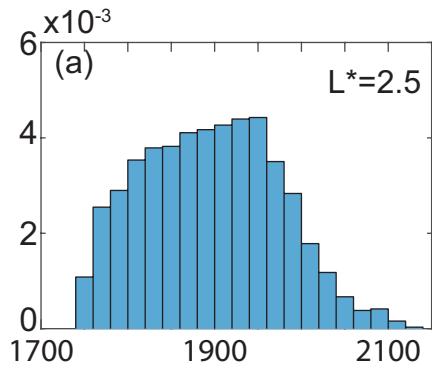


Figure 2.

Probability Distribution Function



— AE < 50 nT

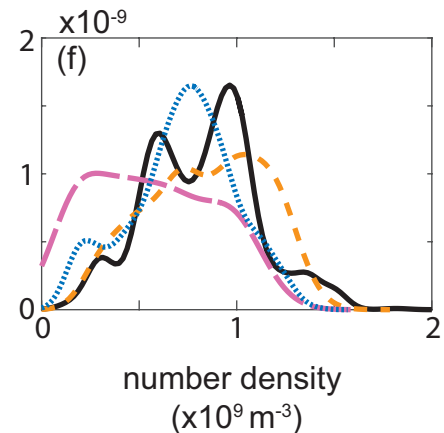
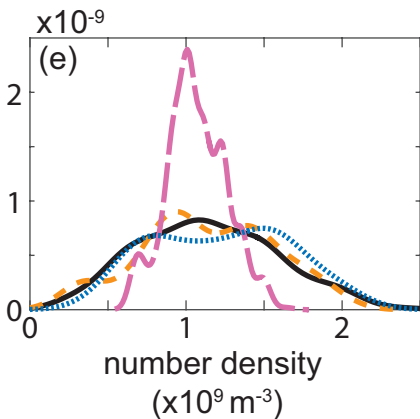
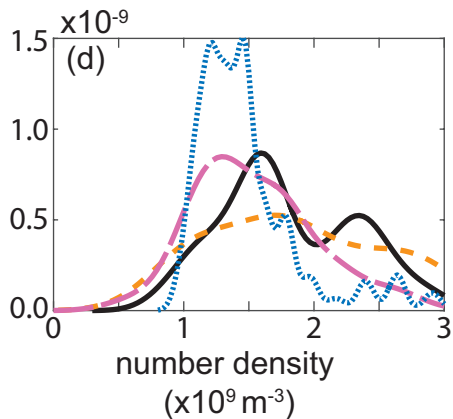
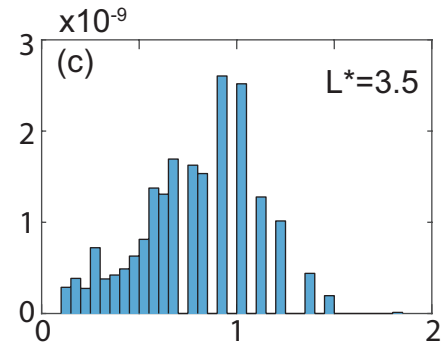
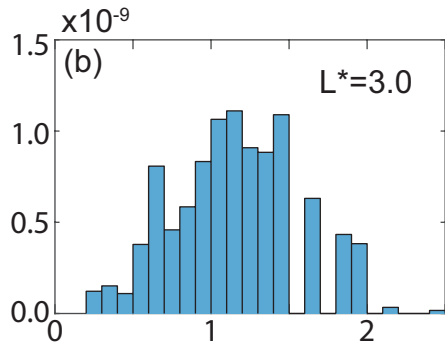
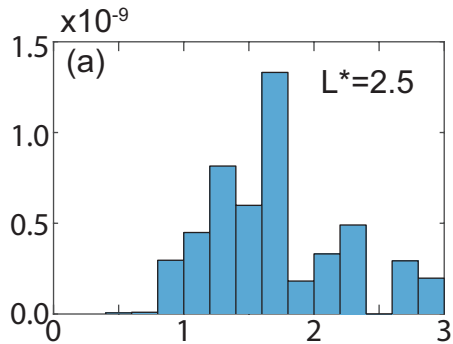
⋯ 50 < AE < 100 nT

- - 100 < AE < 150 nT

- · - AE > 150 nT

Figure 3.

Probability Distribution Function



— AE < 50 nT

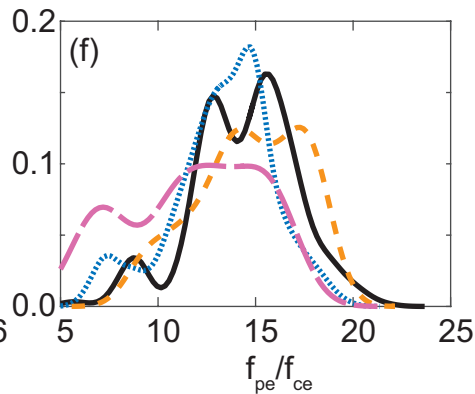
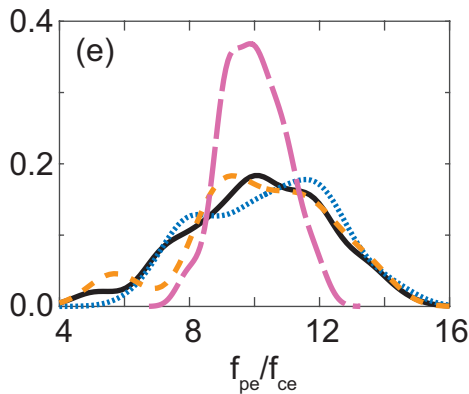
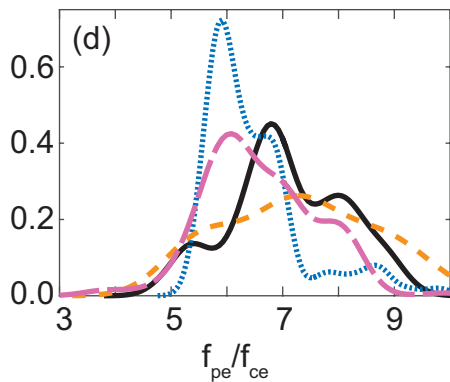
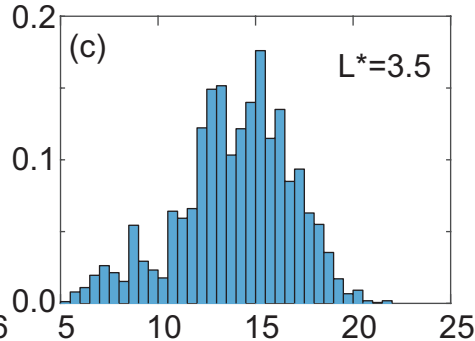
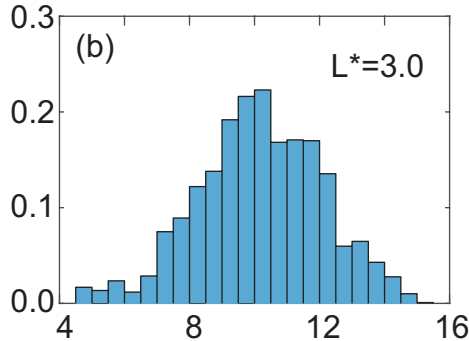
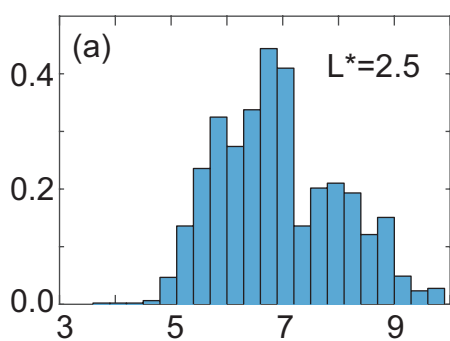
⋯ 50 < AE < 100 nT

- - 100 < AE < 150 nT

- · - AE > 150 nT

Figure 4.

Probability Distribution Function



— AE < 50 nT

⋯ 50 < AE < 100 nT

- - 100 < AE < 150 nT

- · - AE > 150 nT

Figure 5.

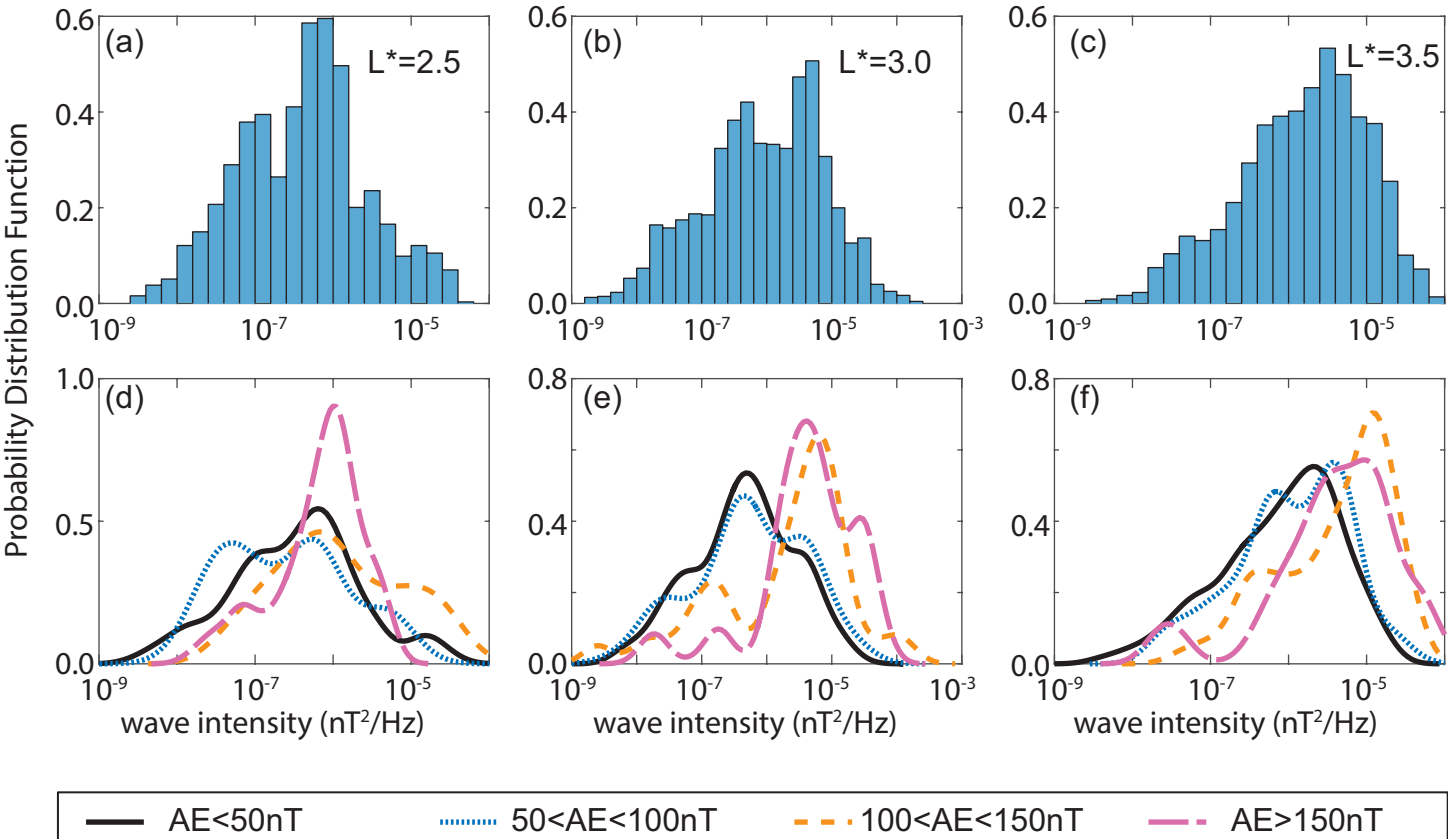


Figure 6.

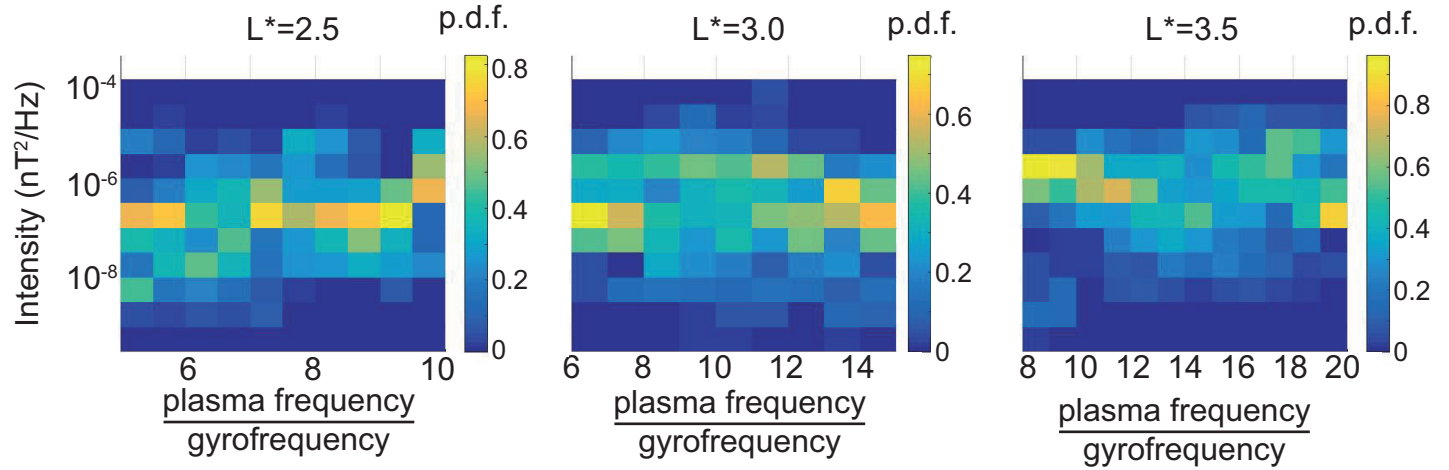
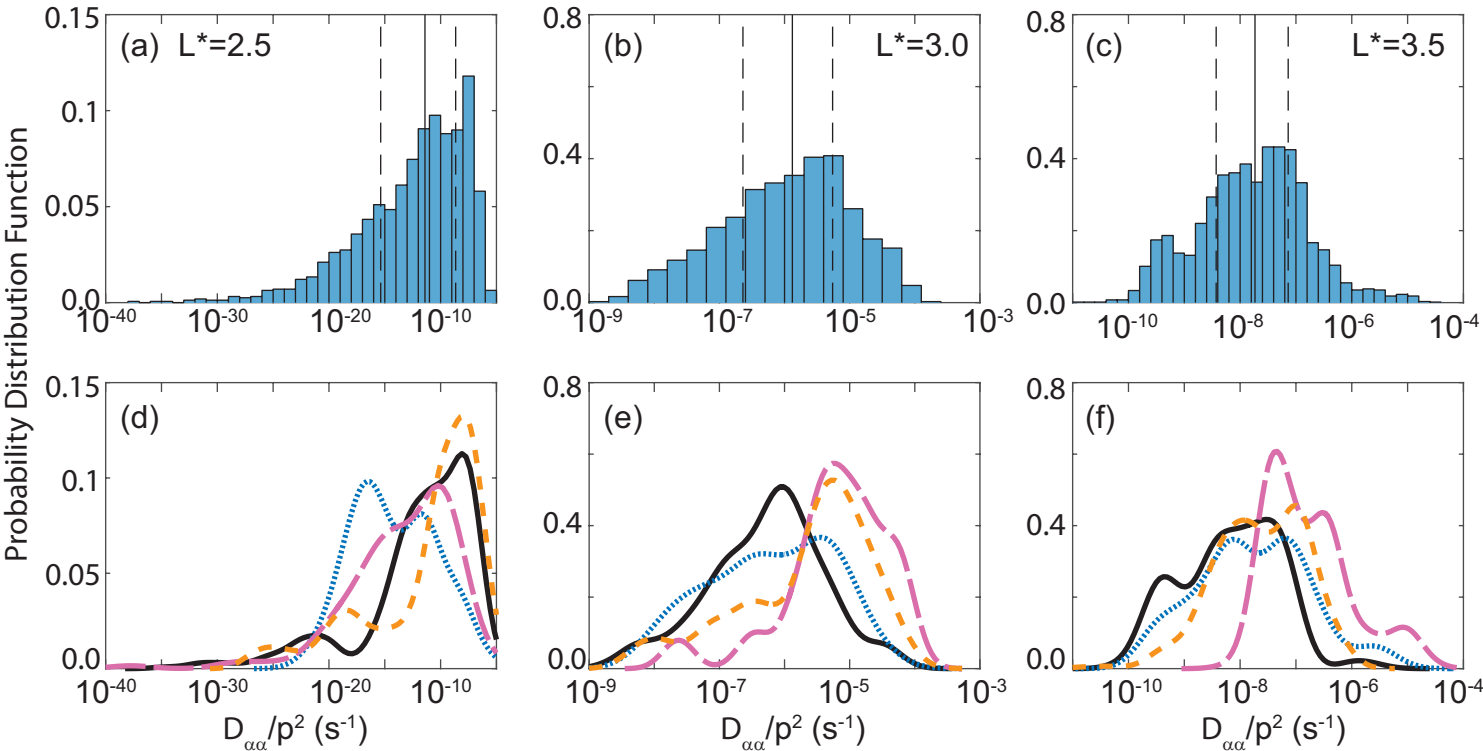


Figure 7.



— AE<50nT

⋯ 50<AE<100nT

- - 100<AE<150nT

- · - AE>150nT

Figure 8.

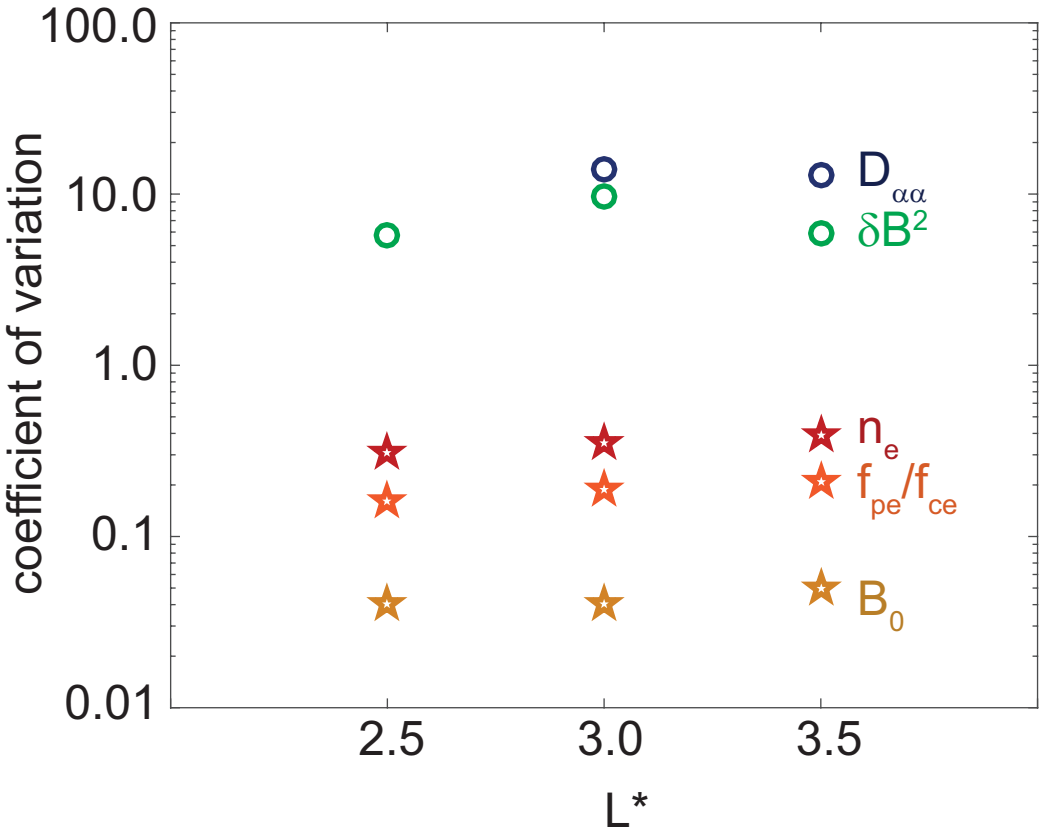


Figure 9.

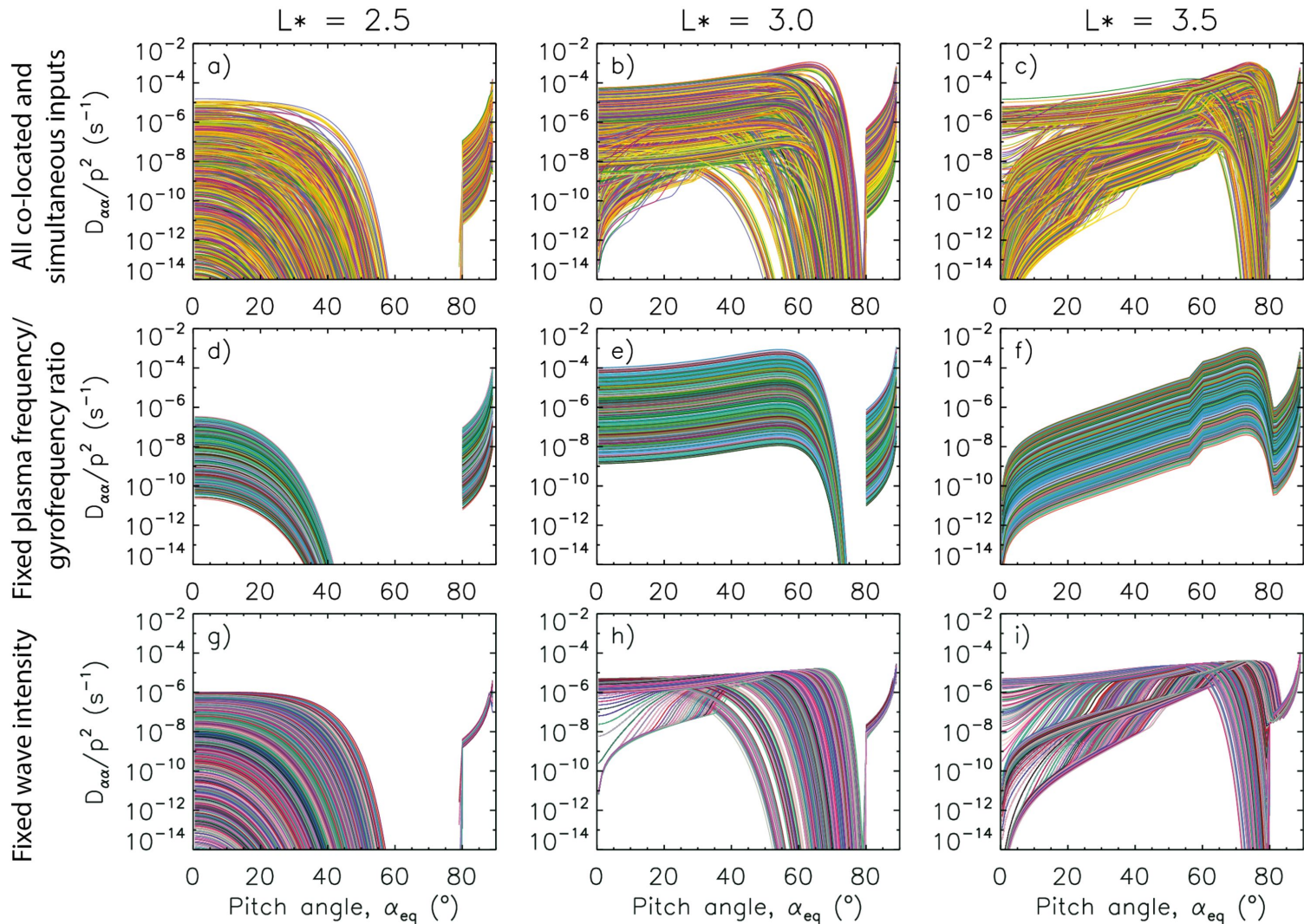
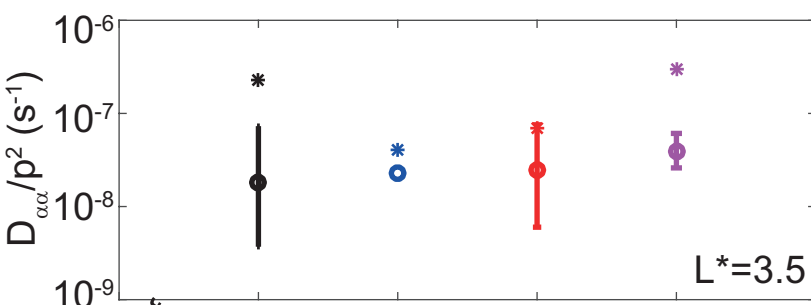
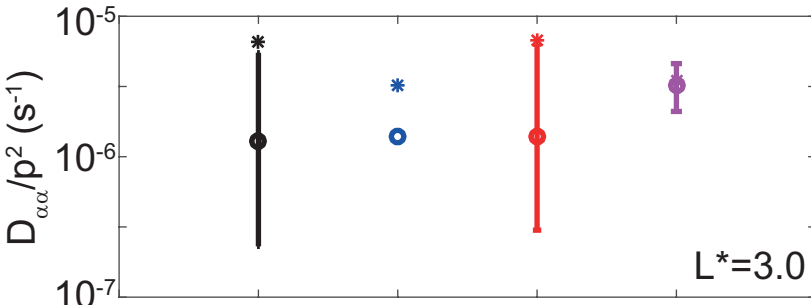
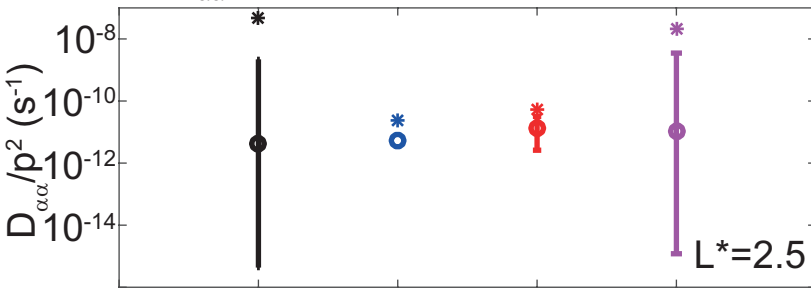


Figure 10.

$D_{\alpha\alpha}$ for $\alpha=30$ degrees, $E=0.5$ MeV

* indicates mean
o indicates median
Ranges are IQR



Full distribution of co-located and simultaneous measurements
 $D_{\alpha\alpha}$ from mean and median δB^2 , f_{pe} / f_{ce}
 Mean f_{pe} / f_{ce}
 All δB^2
 Mean δB^2 , All f_{pe} / f_{ce}